

## Problem Set 6: Analysis of the 2004 Sumatra-Andaman earthquake

### Part 2: Analyzing the effects of rupture complexity and Earth heterogeneity

GEOS 626: Applied Seismology, Carl Tape

Last compiled: October 16, 2017

### SOLUTIONS

## Problem 1 (4.0). Splitting of normal mode frequencies

1. We examine the modes observations listed in *Dziewonski and Anderson* (1981) and in Figure 1 of *Park et al.* (2005). The notation is  $nS_l$ , where  $n$  is the overtone number and  $l$  is the (angular) degree.

- (a) List the toroidal modes, 0.2–1.0 mHz, that were observed in 1980.

$$_0T_2, _0T_3, _0T_4, _0T_5$$

- (b) List the spheroidal modes, 0.2–1.0 mHz, that were observed in 1980.

$$_0S_2, _0S_3, _0S_4, _1S_2, _0S_0, _0S_5, _1S_3, _3S_1$$

- (c) Figure 1 of *Park et al.* (2005) reveals almost all possible modes over the frequency range 0.2–1.0 mHz.  $_2S_1$  does not overlap with other peaks, and it is visible in 2004 but not by 1980. Even toroidal modes are visible ( $_0T_2$ ), though expectedly weak on this vertical component seismogram.  $_0T_3$  and  $_0T_4$  are questionable (but labeled), and  $_0T_5$  is not visible.

Three peaks are superimposed near 0.94 mHz (Table S1).

Table S1: Eigenfrequencies of modes in PREM near 0.94 mHz. The eigenfrequencies are plotted in Figure S1. Note that these three labels are shown above the peak(s) in Figure 1 of *Park et al.* (2005).

mode	$nfl$ , mHz	singlets
$_2S_2$	0.93785	$_2S_2^{-2}, _2S_2^{-1}, _2S_2^0, _2S_2^1, _2S_2^2$
$_1S_3$	0.93983	$_1S_3^{-3}, \dots, _1S_3^3$
$_3S_1$	0.94395	$_3S_1^{-1}, _3S_1^0, _3S_1^1$

The Slichter mode  $_1S_1$ , “one of the last Holy Grails of observational seismology” was not observed for this earthquake (*Okal and Stein*, 2009). This mode has a period of about 4 hours (0.07 mHz); its peak would appear to the left of our 0.2–1.0 mHz range.

- (d) Figure S2 shows eigenfunctions for  $_0S_2$  (lower mantle),  $_1S_2$  (mantle), and  $_2S_2$  (inner core). The sensitivity at the surface for  $_2S_2$  is almost zero, making it extremely difficult to measure this mode at the surface. A second reason that it will be difficult to observe  $_2S_2$  is that it has nearly the same eigenfrequency as  $_1S_3$  and  $_3S_1$  (Table S1). See *Okal and Stein* (2009, Section 7) for details.

2. There are 169 records total, 30 of which were excluded. The 10-day records were excluded from the modes analysis for several possible reasons:

- (a) No obvious earthquake signal (ADK, FUNA, GRFO, LCO, MBWA, PTCN, POHA, RSSD, SHEL, TRIS, XMAS, WAKE).
- (b) Decent direct arrival signal, but problems arise later (DAV, DGAR).  
DGAR has problems shortly after the direct arrival. DAV has problems about 4 days after the earthquake, then severe problems starting at about 5 days after the earthquake.
- (c) Noisy post-earthquake signal (TRISIU).
- (d) Data gaps (OTAV, PNG, SAML, SDV, TRIS).
- (e) Too-strong oscillatory signal (RAO, HOPE).
- (f) Asymmetric peaks after main event (PEL, PALK).

Note that many of these records have problems in multiple categories.

The full list of stations is shown below. The first column ranges from 1 to 169, the second column ranges from 1 to 139 and denotes the page number within the pdf (or the index of the stations that we will pick for analysis).

1	1	AAK	LHZ_00	II	1
2	2	ABKT	LHZ_00	II	1
3	0	ADK	LHZ_00	IU	0
4	3	AFI	LHZ_00	IU	1
5	4	AFI	LHZ_10	IU	1
6	5	AIS	LHZ_00	G	1
7	6	ALE	LHZ_00	II	1
8	7	ALE	LHZ_10	II	1
9	8	ANMO	LHZ_00	IU	1
10	9	ANMO	LHZ_10	IU	1
11	10	ANTO	LHZ_00	IU	1
12	11	ARU	LHZ_00	II	1
13	12	ASCN	LHZ_00	II	1
14	13	ASCN	LHZ_10	II	1
15	14	ATD	LHZ	G	1
16	15	BBSR	LHZ_00	IU	1
17	16	BFO	LHZ_00	II	1
18	17	BILL	LHZ_00	IU	1
19	18	BORG	LHZ_00	II	1
20	19	BORG	LHZ_10	II	1
21	20	BRVK	LHZ_00	II	1
22	21	CAN	LHZ	G	1
23	22	CASY	LHZ_00	IU	1
24	23	CASY	LHZ_10	IU	1
25	24	CCM	LHZ_00	IU	1
26	25	CHTO	LHZ_00	IU	1
27	26	CMLA	LHZ_00	II	1
28	27	COCO	LHZ_00	II	1
29	28	COLA	LHZ_00	IU	1
30	29	COLA	LHZ_10	IU	1
31	30	COR	LHZ_00	IU	1
32	31	CRZF	LHZ_00	G	1
33	32	CTAO	LHZ_00	IU	1
34	0	DAV	LHZ_00	IU	0
35	0	DGAR	LHZ_00	II	0
36	33	DGAR	LHZ_10	II	1
37	34	DRV	LHZ_00	G	1
38	35	DWPF	LHZ_00	IU	1
39	36	ECH	LHZ_00	G	1
40	37	EPI	LHZ_00	II	1
41	38	ESK	LHZ_00	II	1
42	39	FDF	LHZ_00	G	1
43	40	FFC	LHZ_00	II	1
44	0	FUNA	LHZ_00	IU	0
45	0	FUNA	LHZ_10	IU	0
46	41	FURI	LHZ_00	IU	1
47	42	FURI	LHZ_10	IU	1
48	43	GN1	LHZ_00	IU	1
49	0	GRFO	LHZ	IU	0
50	44	GUMO	LHZ_00	IU	1
51	45	GUMO	LHZ_10	IU	1
52	46	HDC	LHZ	G	1
53	47	HKT	LHZ_00	IU	1
54	48	HNR	LHZ_00	IU	1
55	49	HNR	LHZ_10	IU	1
56	0	HOPE	LHZ_00	II	0

57	50	HRV	LHZ	IU	1
58	51	HYB	LHZ	G	1
59	52	INCN	LHZ_00	IU	1
60	53	INCN	LHZ_10	IU	1
61	54	INU	LHZ	G	1
62	55	JTS	LHZ_00	II	1
63	56	KDAK	LHZ_00	II	1
64	57	KDAK	LHZ_10	II	1
65	58	KEV	LHZ_00	IU	1
66	59	KEV	LHZ_10	IU	1
67	60	KIEV	LHZ_00	IU	1
68	61	KIP	LHZ_00	G	1
69	62	KIP	LHZ_10	G	1
70	63	KIP_IU	LHZ_00	IU	1
71	64	KIP_IU	LHZ_10	IU	1
72	65	KIV	LHZ_00	II	1
73	66	KMBO	LHZ_00	IU	1
74	67	KONO	LHZ_00	IU	1
75	68	KONO	LHZ_10	IU	1
76	69	KURK	LHZ_00	II	1
77	70	KWAJ	LHZ_00	II	1
78	0	LCO	LHZ	IU	0
79	71	LSZ	LHZ_00	IU	1
80	72	LSZ	LHZ_10	IU	1
81	73	LVC	LHZ_00	IU	1
82	74	LVC	LHZ_10	IU	1
83	75	LVZ	LHZ_00	II	1
84	76	MA2	LHZ_00	IU	1
85	77	MAJO	LHZ_00	IU	1
86	78	MBAR	LHZ_00	II	1
87	79	MBO	LHZ_00	G	1
88	0	MBWA	LHZ_00	IU	0
89	80	MBWA	LHZ_10	IU	1
90	81	MIDW	LHZ_00	IU	1
91	82	MPG	LHZ_00	G	1
92	83	MSEY	LHZ_00	II	1
93	84	NNA	LHZ_00	II	1
94	85	NWAO	LHZ_00	IU	1
95	86	OBN	LHZ_00	II	1
96	0	OTAV	LHZ_00	IU	0
97	0	OTAV	LHZ_10	IU	0
98	87	PAB	LHZ_00	IU	1
99	88	PAF	LHZ_00	G	1
100	0	PALK	LHZ_00	II	0
101	89	PAYG	LHZ_00	IU	1
102	90	PAYG	LHZ_10	IU	1
103	0	PEL	LHZ	G	0
104	91	PET	LHZ_00	IU	1
105	92	PFO	LHZ_00	II	1
106	93	PFO	LHZ_10	II	1
107	0	PMG	LHZ_00	IU	0
108	0	PMG	LHZ_10	IU	0
109	94	PMSA	LHZ_00	IU	1
110	0	POHA	LHZ_00	IU	0
111	95	POHA	LHZ_10	IU	1
112	96	PPT	LHZ	G	1
113	0	PTCN	LHZ_00	IU	0
114	97	QSPA	LHZ_00	IU	1
115	98	QSPA	LHZ_10	IU	1
116	99	QSPA	LHZ_20	IU	1
117	100	QSPA	LHZ_30	IU	1
118	0	RAO	LHZ_00	IU	0
119	101	RAO	LHZ_10	IU	1
120	102	RAR	LHZ_00	IU	1
121	103	RAR	LHZ_10	IU	1
122	104	RAYN	LHZ_00	II	1
123	105	RCBR	LHZ_00	IU	1
124	106	RCBR	LHZ_10	IU	1
125	107	RER	LHZ_00	G	1
126	108	RPN	LHZ_00	II	1
127	109	RPN	LHZ_10	II	1
128	0	RSSD	LHZ_00	IU	0
129	0	SAML	LHZ_00	IU	0
130	0	SAML	LHZ_10	IU	0
131	110	SBA	LHZ_00	IU	1
132	111	SCZ	LHZ	G	1
133	0	SDV	LHZ_00	IU	0
134	0	SDV	LHZ_10	IU	0
135	112	SFJ	LHZ_00	IU	1
136	0	SHEL	LHZ_00	II	0
137	113	SJG	LHZ_00	IU	1
138	114	SNZO	LHZ_00	IU	1
139	115	SNZO	LHZ_10	IU	1
140	116	SSB	LHZ_00	G	1
141	117	SSPA	LHZ_00	IU	1
142	118	SUR	LHZ_00	II	1
143	119	TAM	LHZ	G	1
144	120	TATO	LHZ_00	IU	1
145	121	TATO	LHZ_10	IU	1
146	122	TAU	LHZ_00	II	1
147	123	TEIG	LHZ_00	IU	1
148	124	TEIG	LHZ_10	IU	1
149	125	TIXI	LHZ_00	IU	1
150	126	TLY	LHZ_00	II	1
151	0	TRIS	LHZ_00	G	0
152	0	TRIS	LHZ_10	G	0
153	0	TRISIU	LHZ_00	IU	0
154	0	TRISIU	LHZ_10	IU	0

```

155 127 TRQA LHZ_00 IU 1
156 128 TRQA LHZ_10 IU 1
157 129 TUC LHZ_00 IU 1
158 130 ULN LHZ_00 IU 1
159 131 UNM LHZ G 1
160 0 WAKE LHZ_00 IU 0
161 132 WAKE LHZ_20 IU 1
162 133 WCI LHZ_00 IU 1
163 134 WRAB LHZ_00 II 1
164 135 WRAB LHZ_10 II 1
165 136 WUS LHZ_00 G 1
166 137 WWT LHZ IU 1
167 0 XMAS LHZ_00 IU 0
168 138 YAK LHZ_00 IU 1
169 139 YSS LHZ_00 IU 1

```

3. (a) I kept 60 stations that all had decent signal-to-noise for the  ${}_0S_2$  peak at 0.3093 mHz (3233.25 s, *Dziewonski and Anderson*, 1981, Table V). The distribution of stations is plotted in Figure S3.
- (b) A histogram of the  ${}_0S_0$  amplitudes is plotted in Figure S4. The median value is 10.3. Considering only the cluster of values above 9, the standard deviation is approximately 1. The best way to determine the amplitudes would be to deconvolve the instrument response. Here we have only applied the calibration factor, for simplicity. Still, deconvolving the instrument response may not explain the outliers in the histogram. *Rosat et al.* (2007) discussed the amplitude variations of  ${}_0S_0$  in the context of theoretical predictions that amplitudes are 2% higher at the pole than at the equator. Their analysis uses 13 superconducting gravimeters, not broadband seismometers, and they examined longer time series (their 34 days versus our 10 days).
4. (a) Figure S5 shows the stacked spectrum for the 2004 Sumatra earthquake.
- (b) **Recall that these are vertical component seismograms.** Each spike represents a discrete frequency of a specific spheroidal mode (though we know that some toroidal modes are visible). The frequencies can be well predicted by a one-dimensional Earth model such as PREM. Each frequency is associated with a mode that has a specific spatial variation on Earth (nodal lines on the surface; nodes in the radial/vertical direction), with the point of symmetry at the location of the earthquake. The relative amplitudes of the peaks depend on the earthquake source parameters, notably the depth and radiation pattern. The exquisite quality of this spectrum is primarily due to the immense magnitude ( $M_w$  9.2) of the Sumatra earthquake.
5. (a) Figure S6 shows the stack for  ${}_0S_2$ . The relevant code leading to Figure S6 is

```

% OS2 splitting parameters from stack
% frequency interval to plot/interpolate, in mHz
T0 = 3233.25; f0 = 1/T0*1e3; n=0; l=2;
stit = sprintf('_%iS_%i (n=%i, l=%i): f = %.4f mHz, T = %.2f min',n,l,n,l,f0,T0/60);
disp(stit);
f1 = f0 - 0.04;
f2 = f0 + 0.04;
nv = 1000;
[Avstack,fv,Av] = w2fstack(w,f1*1e-3,f2*1e-3,nv);

```

```

figure; nr=2; nc=1;
subplot(nr,nc,1); plot(fv*1e3,Av); xlim([f1 f2]); xlabel('Frequency, mHz');
subplot(nr,nc,2); hold on;
plot(fv*1e3,Avstack); xlim([f1 f2]); xlabel('Frequency, mHz'); title(stit);

```

- (b) The peaks from left to right in Figure S6 are  ${}_0S_2^{-2}$ ,  $\dots$ ,  ${}_0S_2^2$ .
- (c) For the gravest modes (including  ${}_0S_2$ ), the frequency deviation of the  $m$ th singlet from the  $m = 0$  degenerate frequency can be computed as (*Dahlen and Tromp*, 1998, Eq. 14.54)

$$\delta\omega_m = \omega_0(a + bm + cm^2) \quad -l \leq m \leq l, \quad (\text{S1})$$

where expressions for  $a$  and  $c$  are primarily associated with ellipticity (but also large-scale structure), and  $b$  is associated with rotation. We can rewrite this as

$$f_m - f_0 = f_0(a + bm + cm^2) \quad (\text{S2})$$

$$f_m = f_0(1 + a + bm + cm^2) \quad (\text{S3})$$

We use the more explicit notation  $f_0 \equiv {}_0f_l^m$ . Our measured values and linear model are

$${}_0f_2^0 = 0.309 \text{ mHz} \quad (\text{S4})$$

$$\Delta f = 0.0046 \text{ mHz} \quad (\text{S5})$$

$${}_0f_2^m = {}_0f_2^0 + m\Delta f, \quad m = -2, -1, 0, 1, 2 \quad (\text{S6})$$

In comparison with Equation (S3), we have the coefficients

$$a = 0$$

$$b = \Delta f / {}_0f_2^0 = 14.9 \times 10^{-3}$$

$$c = 0$$

For comparison, the splitting parameters for  ${}_0S_2$  for Earth model 1066A (*Gilbert and Dziewonski*, 1975) are (*Dahlen and Tromp*, 1998, Table 14.1)

$$a = 0.376 \times 10^{-3}$$

$$b = 14.905 \times 10^{-3}$$

$$c = -0.267 \times 10^{-3}$$

The quadratic term plays a minimal role in the fitting, as shown in Figure S7.

6. Figure S8 shows the  ${}_0S_2$  spectra sorted by latitude. The most conspicuous pattern is that the singlets disappear at high latitudes, the best examples being QSPA ( $\lambda = -89.93^\circ$ ) and ALE ( $\lambda = 82.53^\circ$ ). This shows that the splitting of  ${}_0S_2$  is primarily controlled by some property with variations in latitude. Since we can rule out large-scale Earth structure, we are left with rotation and ellipticity. The effects of the Earth's 24-hour rotation turn out to be more significant than its ellipticity.

*Stein and Okal* (2007, Figure 3) wrote, “Note the control of the splitting pattern by receiver latitude,” but no detailed explanation is provided. From Figure S8, we can see striking symmetry across the equator. Generally speaking, the number of dominant peaks ranges from 1 for latitudes  $|\lambda| > 60^\circ$ , to 5 peaks for  $40^\circ < |\lambda| < 60^\circ$ , to 2 (or 4) peaks for  $30^\circ < |\lambda| < 40^\circ$ , to 3 peaks for  $|\lambda| < 30^\circ$ .

7. (a) There are two nodal “latitudes” (more appropriate: “small circles”) for  ${}_0S_2$ , as illustrated in Figure 2.9-7 of *Stein and Wysession* (2003). These nodal lines occur at epicentral distances

$$\Delta_1 = \cos^{-1}(1/\sqrt{3}) \approx 54.7^\circ \quad (\text{S7})$$

$$\Delta_2 = \cos^{-1}(-1/\sqrt{3}) \approx 125.3^\circ \quad (\text{S8})$$

These distances are denoted by the dashed lines in Figure S9.

If the excitation were a point source and the Earth was SNREI<sup>1</sup>, then we would expect very low amplitudes of  ${}_0S_2$  at stations near  $\Delta_1$  and  $\Delta_2$ . The number of peaks and their relative amplitudes do not seem to depend on  $\Delta$ .

- (b) Figure S9 shows the  ${}_0S_2$  spectra sorted by epicentral distance.

In Figure S10 I plot the amplitude of the singlet  ${}_0S_2^0$  as a function of epicentral distance, and **I do not see any pattern**. It is true that the highest amplitudes appear at  $\Delta = 90^\circ$ , and the lowest amplitudes appear near the nodal lines, but overall the observations do not support the theoretical expectations for a spherically symmetric earth model.

## 8. Radial modes ( $l = 0$ ).

- (a) Figure S11 shows plots of the Sumatra spectrum in the vicinity of the expected peaks for the radial modes  ${}_0S_0$ ,  ${}_1S_0$ ,  ${}_2S_0$ ,  ${}_3S_0$ , and  ${}_4S_0$ . All frequencies listed are from PREM, Table V.

- ${}_0S_0$ . This is the fundamental radial mode (0.8147 mHz), also known as the “breathing mode.”
- ${}_1S_0$ . This is the first radial overtone (1.6313 mHz).
- ${}_2S_0$ . This is the second radial overtone (2.5091 mHz). It may be barely visible, but it is also coupled to the core-sensitive mode  ${}_7S_2$  (2.5165 mHz) (*Durek and Ekström*, 1995), which is probably the larger of the two small peaks visible.
- ${}_3S_0$ . This is the third radial overtone (3.2697 mHz). This is not visible; the large visible peak is  ${}_0S_{24}$  (3.2658 mHz).
- ${}_4S_0$ . This is the fourth radial overtone (4.1039 mHz). This is not visible; the large visible peak is  ${}_0S_{33}$  (4.0836 mHz). The mode  ${}_{10}S_2$  couples to  ${}_4S_0$ .

- (b) What is significant about these peaks is that **they are not split** by rotation, ellipticity, or large-scale 3D structure variations. These  $l = 0$  modes are called *radial modes*

---

<sup>1</sup>SNREI = Spherically symmetric, non-rotating, perfectly elastic and isotropic. See *Dahlen and Tromp* (1998, Section 8.2).

because they involve only radial motion. While the motion of the  ${}_0S_0$  “breathing mode” is intuitive, the motions of the radial overtones ( ${}_nS_l$ ) are not. Figure 2.9-7 of *Stein and Wysession* (2003) shows an example of  ${}_1S_0$ . It is perhaps best to think of the nodal spherical surfaces for these nodes ( $n$  surfaces for  ${}_nS_0$ ), where motion oscillates in opposite directions on either side of the fixed surface. Another way to show degeneracy is that, with  $l = 0$ , we must have  $m = 0$  since  $-l \leq m \leq l$ .

Low-angle faults, like the Sumatra earthquake, do not excite radial modes well. By comparison, the smaller ( $M_w$  8.2) deep (647 km) Bolivia earthquake of 1994–June–09 strongly excited the Earth’s radial modes. These modes were used by *Durek and Ekström* (1995) to determine the bulk attenuation in the asthenosphere.

## Problem 2 (4.0). Directivity

1. NA
2. We will repeat the analysis of *Ni et al.* (2005) but using even more simplifications than they did. Figure S12 shows that velocity really isn’t constant as a function of distance (as we know). We could easily have made a distance-based correction for velocity, as done in *Ni et al.* (2005).

First, we need to derive  $T_r$  (*Stein and Wysession*, 2003, Section 4.3.2):

$$T_r(\alpha) = L \left( \frac{1}{v_r} - \frac{\cos(\alpha - \alpha_0)}{v} \right) \quad (\text{S9})$$

A geometrical approximation is needed. As stated, the law of cosines gives us (SW eq. 6)

$$r^2 = r_0^2 + L^2 - 2 r_0 L \cos \theta \quad (\text{S10})$$

We are then told that for  $r \gg L$  (SW eq. 7)

$$r \approx r_0 - L \cos \theta \quad (\text{S11})$$

(Here we’ll use  $\theta = \alpha - \alpha_0$ .) Let’s at least check these equations, since it is not obvious. First we assume that  $\theta$  is fixed. (There may be a more general way to derive this when  $\theta$  is varying.) Next we want to show that  $\lim_{r_0 \rightarrow \infty} (r[\text{SWeq6}] - r[\text{SWeq7}]) = 0$ . We rewrite

the difference of these equations:

$$\begin{aligned}
r[\text{SWeq6}] - r[\text{SWeq7}] &= \sqrt{r_0^2 + L^2 - 2r_0L \cos \theta} - (r_0 - L \cos \theta) \\
&= L \cos \theta + \sqrt{r_0^2 + L^2 - 2r_0L \cos \theta} - r_0 \\
&= L \cos \theta + \left( \sqrt{r_0^2 + L^2 - 2r_0L \cos \theta} - r_0 \right) \frac{\sqrt{r_0^2 + L^2 - 2r_0L \cos \theta} + r_0}{\sqrt{r_0^2 + L^2 - 2r_0L \cos \theta} + r_0} \\
&= L \cos \theta + \frac{r_0^2 + L^2 - 2r_0L \cos \theta - r_0^2}{r_0 + \sqrt{r_0^2 + L^2 - 2r_0L \cos \theta}} \\
&= L \cos \theta + \frac{L^2 - 2r_0L \cos \theta}{r_0 + \sqrt{r_0^2 + L^2 - 2r_0L \cos \theta}} \frac{1/r_0}{1/r_0} \\
&= L \cos \theta + \frac{\frac{L^2}{r_0} - 2L \cos \theta}{1 + \sqrt{1 + \left(\frac{L}{r_0}\right)^2 - \frac{2L \cos \theta}{r_0}}}
\end{aligned}$$

Applying the limit, we have

$$\begin{aligned}
\lim_{r_0 \rightarrow \infty} (r[\text{SWeq6}] - r[\text{SWeq7}]) &= \lim_{r_0 \rightarrow \infty} \left[ L \cos \theta + \frac{\frac{L^2}{r_0} - 2L \cos \theta}{1 + \sqrt{1 + \left(\frac{L}{r_0}\right)^2 - \frac{2L \cos \theta}{r_0}}} \right] \\
&= L \cos \theta + \frac{-2L \cos \theta}{1 + \sqrt{1}} \\
&= 0
\end{aligned}$$

Therefore the approximation used in SW eq. 7 (Eq. S11 above) is okay. (If you see a simpler way to demonstrate the validity of Eq. S11, let me know!)

The apparent rupture time,  $T_r$ , is a function of station azimuth,  $\alpha$ , with respect to the rupture azimuth,  $\alpha_0$ . Let  $t_b$  represent the time it takes for the waves at the start of the rupture to reach the station. Let  $t_e$  represent the time it takes waves at the end of the rupture to reach the station. Then the apparent rupture time is

$$T_r(\alpha) = t_e - t_b \quad (\text{S12})$$

$$= \left( \frac{L}{v_r} + \frac{r}{v} \right) - \frac{r_0}{v} \quad (\text{S13})$$

$$= \frac{L}{v_r} + \frac{r}{v} - \frac{r + L \cos(\alpha - \alpha_0)}{v} \quad (\text{S14})$$

$$= L \left( \frac{1}{v_r} - \frac{\cos(\alpha - \alpha_0)}{v} \right) \quad (\text{S15})$$

where  $v_r$  is the rupture velocity,  $v = 11$  km/s is the velocity of the medium,  $L$  is the fault length,  $\alpha$  is the azimuth to the station,  $\alpha_0$  is the rupture direction, and the key substituition

is to use Equation (S11) for  $r_0$ .

- (a) The actual rupture time is  $L/v_r$ .
  - (b) The actual rupture time matches the apparent rupture time for a station perpendicular to the fault ( $\alpha = \alpha_0 \pm 90^\circ$ ):
- $$T_{\perp} = T_r(\alpha_0 \pm 90^\circ) = L \left( \frac{1}{v_r} - \frac{\cos(\alpha - \alpha_0)}{v} \right) = L \left( \frac{1}{v_r} - \frac{\cos(\pm 90^\circ)}{v} \right) = \frac{L}{v_r} \quad (\text{S16})$$
- (c) The minimum apparent rupture time occurs in the direction of rupture,  $\alpha = \alpha_0$ .
  - (d) The maximum apparent rupture time occurs in the direction opposite to the rupture direction,  $\alpha = \alpha_0 + 180^\circ$ .
  - (e) The maximum value, minimum value, and range are

$$T_{\max} \equiv T_r(\alpha_0 + 180^\circ) = L \left( \frac{1}{v_r} + \frac{1}{v} \right) \quad (\text{S17})$$

$$T_{\min} \equiv T_r(\alpha_0) = L \left( \frac{1}{v_r} - \frac{1}{v} \right) \quad (\text{S18})$$

$$T_{\text{range}} = T_{\max} - T_{\min} = \frac{2L}{v} \quad (\text{S19})$$

So the azimuthal variation in  $T_r$  is *not* a function of rupture velocity.

- (f) The azimuthal average of  $T_r$  can be calculated as the mean over all angles:

$$\begin{aligned} \bar{T}_r &= \frac{1}{2\pi} \int_0^{2\pi} L \left( \frac{1}{v_r} - \frac{\cos(\alpha - \alpha_0)}{v} \right) d\alpha \\ &= \frac{1}{2\pi} \left[ \frac{L}{v_r} \alpha \Big|_0^{2\pi} - \frac{1}{v} \sin u \Big|_{\alpha_0}^{\alpha_0+2\pi} \right] \\ &= \frac{L}{v_r} \end{aligned} \quad (\text{S20})$$

So the azimuthal average of  $T_r$  is *not* a function of the velocity of the medium.

It is equal to the actual rupture time, which supports our intuition.

(g) Our 3 equations with 8 unknowns ( $T_r$ ,  $L$ ,  $v_r$ ,  $v$ ,  $\alpha$ ,  $\alpha_0$ ,  $T_{\max}$ ,  $T_{\min}$ ) are

$$T_r(\alpha) = L \left( \frac{1}{v_r} - \frac{\cos(\alpha - \alpha_0)}{v} \right) \quad (\text{S21})$$

$$T_{\max} = L \left( \frac{1}{v_r} + \frac{1}{v} \right) \quad (\text{S22})$$

$$T_{\min} = L \left( \frac{1}{v_r} - \frac{1}{v} \right) \quad (\text{S23})$$

From these we have

$$\frac{T_{\max} - T_{\min}}{2} = \frac{1}{2} \left( L \left( \frac{1}{v_r} + \frac{1}{v} \right) - L \left( \frac{1}{v_r} - \frac{1}{v} \right) \right) = \frac{L}{v}$$

$$\frac{T_{\max} + T_{\min}}{2} = \frac{1}{2} \left( L \left( \frac{1}{v_r} + \frac{1}{v} \right) + T_{\min} + L \left( \frac{1}{v_r} - \frac{1}{v} \right) \right) = \frac{L}{v_r}$$

We use these to reduce our 3 equations to 1 equation with 5 unknowns ( $T_r$ ,  $T_{\min}$ ,  $T_{\max}$ ,  $\alpha$ ,  $\alpha_0$ ):

$$\begin{aligned} T_r(\alpha) &= L \left( \frac{1}{v_r} - \frac{\cos(\alpha - \alpha_0)}{v} \right) \\ &= \frac{L}{v_r} - \frac{L}{v} \cos(\alpha - \alpha_0) \\ &= \frac{1}{2} [(T_{\max} + T_{\min}) - (T_{\max} - T_{\min}) \cos(\alpha - \alpha_0)] \end{aligned}$$

So the azimuthal variation in apparent rupture time,  $T_r(\alpha)$ , can be estimated directly from three measurements:  $T_{\min}$ ,  $T_{\max}$ , and  $\alpha_0$  (the azimuth with the minimum apparent rupture time).

3. Figure S13 reproduces the analysis of *Ni et al.* (2005, Figure 1d).

See also *Ammon et al.* (2005, Figure 1), which highlights “three relatively energetic amplitude bursts” that also exhibit the azimuthal pattern.

4. I did not specify whether you should select  $\alpha_0$  based on your analysis or based on *Ni et al.* (2005), who used  $\alpha_0 = 340^\circ$ . This will not impact your answer.

Three stations with the **smallest**  $T_r$ , therefore in the azimuthal direction  $\alpha_0$ , are BRVK.II ( $341^\circ$ ), KURK.II ( $346^\circ$ ), and TLY.II ( $6^\circ$ ) (Figure S14).

Three stations with the **largest**  $T_r$ , therefore in the azimuthal direction  $\alpha_0 + 180^\circ$ , are CASY.IU ( $174^\circ$ ), PAF.G ( $200^\circ$ ), and CRZF.G ( $212^\circ$ ) (Figure S15). Notice that CAN also made the list of few stations toward the south. All of the stations in Figure S15 have clear high-frequency energy in the time range 500–700 s, unlike the stations to the north in Figure S14.

5. Based on Figure S13, I estimate

$$T_{\min} = 500 \text{ s} \quad (\text{S24})$$

$$T_{\max} = 700 \text{ s} \quad (\text{S25})$$

We identify  $\alpha_0 = 0^\circ$  based on  $T_{\min} = T_r(\alpha_0)$ . The other quantities follow (with  $v =$

11 km/s):

$$\alpha_0 = 0^\circ \quad (\text{S26})$$

$$\bar{T}_r = (T_{\max} + T_{\min})/2 = 600 \text{ s} \quad (\text{S27})$$

$$L = (T_{\max} - T_{\min})v/2 = 1100 \text{ km} \quad (\text{S28})$$

$$v_r = L/\bar{T}_r = 1.8 \text{ km/s} \quad (\text{S29})$$

For comparison, the values in *Ni et al.* (2005) are

$$\alpha_0 = 340^\circ$$

$$\bar{T}_r = 500 \text{ s}$$

$$L = 1200 \text{ km}$$

$$v_r = 2.5 \text{ km/s}$$

(What we really need to have are some realistic uncertainties associated with these quantities.)

6. (a) Figures S16–S17

(b) Figures S16–S19 extends the long-period directivity analysis illustrated in Figure S1 of *Ammon et al.* (2005). They used three stations with similar epicentral distances: OBN, YSS, and SBA. These stations have very different azimuths, and they all have epicentral distances  $60^\circ < \Delta < 90^\circ$ :

	az	dist
YSS	36.1	60.5
SBA	168.4	89.3
OBN	328.8	69.5

We use these three stations plus all others with  $60^\circ < \Delta < 90^\circ$  (Figure S16).

An azimuthal record section of seismograms filtered between 200–500 s reveals a striking pattern of the amplitude ratio R2 (major orbit Rayleigh wave) to R1 (minor orbit Rayleigh wave). We can compute the amplitude ratio more easily by using the **envelope of the seismograms** (Figure S18). In Figure S19 we plot the quantity

$$R = \ln(A_{\text{R1}}/A_{\text{R2}}). \quad (\text{S30})$$

For example,  $R = 0$  would mean that the amplitude of R1 and R2 are the same, and  $R < 0$  would indicate that the amplitude of R1 is less than the amplitude of R2 (despite attenuation<sup>2</sup>). I approximated the pattern of observations with a periodic triangle function. The minimum amplitude ratio occurs at  $130^\circ$ ; the maximum occurs in the direction of  $310^\circ$ , which approximates the rupture direction.

---

<sup>2</sup>For stations with these epicentral distances, the R2 path is about 3 times as long as the R1 path. So you would expect the amplitudes to attenuate more for R2. For these waveforms we see that the source directivity has a far greater impact on the amplitudes than attenuation does.

Figures S20–S22 repeat the analysis in Figures S17–S19, but using the period range 500–1000 s. The R2 arrival is not easy to identify (Figure S22), and the amplitude ratios are not as well fit with a triangle function.

- (c) My estimate for the rupture direction was  $\alpha_0 = 0^\circ$  based on the duration of high-frequency (2–4 Hz) P waves, and it was  $\alpha_0 = 310^\circ$  based on the R1/R2 amplitude ratio for long-period (200–500 s) Rayleigh waves. The difference of  $50^\circ$  seems larger than the uncertainties in the respective measurements, so what might be going on here? Looking at the map in Figure 1 (as suggested in the hint) and reading the associated study (*Ammon et al.*, 2005), it seems that the most plausible explanation is that the dominant long-period and short-period energy of this earthquake were released differently. The bulk of the long-period energy was released during the large slip patch near the south, along the northwest-oriented portion of the subduction zone. The duration of the high-frequency P wave energy is related to the full length of the rupture, which is directed due north.

It was not until later, with the 2011 Tohoku-Oki  $M_w$  9.0 earthquake (*Simons et al.*, 2011), that seismologists conclusively showed that large earthquakes could release different frequency energy from different regions of the fault.

### Problem 3 (2.0). Miscellaneous

1. *The importance of deconvolving instrument response.*

Table S2: Comparison between our displacement values—the ones not in parentheses—and the values in Figure S12 of *Ammon et al.* (2005). All values are in mm. The values for DGAR suggest that H1 is N (not E) and H2 is E (not N); these directions are not listed in *Ammon et al.* (2005).

station	E	H1	N	H2	Z	U-D
PALK	–	(–)	–	(59.6)	47.9	(51.1)
COCO	–	(19.5)	–	(9.6)	14.4	(14.5)
HYB	36.1	(–)	50.1	(–)	24.1	(–)
DGAR	25.7	(20.5)	20.7	(25.2)	34.7	(33.3)

- Figure S23 shows a map of the only stations (in our data set) within  $\Delta < 30^\circ$  that have “reasonable” waveforms. Figure S24 shows a record section of filtered waveforms (50–500 s) with calibration applied (`iprocess=1`).
- Figure S25 shows a record section of filtered waveforms with instrument deconvolved (`iprocess=2`).

- (c) A comparison between Figure S24 and Figure S25 reveals major differences when deconvolving the instrument response. Furthermore, the amplitudes are quite different for the two cases (e.g., 27.9 mm vs 47.9 mm for PALK):

```

iprocess = 1
COCO II LHZ_00 -- max 7.6 mm
DGAR II LHZ_10 -- max 19.9 mm
HYB G LHZ -- max 19.7 mm
PALK II LHZ_00 -- max 27.9 mm
DGAR II LHE_10 -- max 14.6 mm
HYB G LHE -- max 35.5 mm
DGAR II LHN_10 -- max 13.6 mm
HYB G LHN -- max 46.0 mm

iprocess = 2
COCO II LHZ_00 -- max 14.4 mm
DGAR II LHZ_10 -- max 34.7 mm
HYB G LHZ -- max 24.1 mm
PALK II LHZ_00 -- max 47.9 mm
DGAR II LHE_10 -- max 25.7 mm
HYB G LHE -- max 36.1 mm
DGAR II LHN_10 -- max 20.7 mm
HYB G LHN -- max 50.1 mm

```

- (d) Upon comparison of Figures S24 and S25 (and the measured amplitudes) with Figure S12 of *Ammon et al.* (2005), we can conclude that the published waveforms had had the instruments deconvolved (as we should expect!).

A comparison between our instrument-deconvolved displacements values with those of *Ammon et al.* (2005) is shown in Table S2. There are certainly some discrepancies that might be due to differences in the type of filter used.

2. (a) Figure S27 reproduces the azimuthal record section in Figure S11 of *Ammon et al.* (2005). Although the authors do not list what bandpass was used, it is probably close to 10–500 s, what we used. (We are also not told what component they used; we assume it is the vertical component.) Another version is plotted in Figure S28.
- (b) We can make several observations from Figure S27:
  - i. There is clear correlation between waveforms with similar azimuths.
  - ii. We see the pattern that the overall amplitudes are smallest in the azimuthal direction of about 180° (e.g., SBA.IU, CASY.IU), opposite to the rupture direction.
  - iii. The “first motion” changes from “down” for stations with azimuths of  $\alpha=150\text{--}300^\circ$  to “up” at other azimuthal angles.
  - iv. Two very long period pulses are present in the direction of  $\alpha \approx 260^\circ$ , the three African stations to the west. It is unclear how these arise.
3. The six stations are: INU.G, CAN.G., TAM.G., SCZ.G, MPG.G, PEL.G. All are Geoscope network stations. See solution at the end of this pdf.

## References

- Ammon, C. J., et al. (2005), Rupture process of the 2004 Sumatra-Andaman earthquake, *Science*, 308, 1133–1139.
- Dahlen, F. A., and J. Tromp (1998), *Theoretical Global Seismology*, Princeton U. Press, Princeton, New Jersey, USA.
- Durek, J. J., and G. Ekström (1995), Evidence of bulk attenuation in the asthenosphere from recordings of the Bolivia earthquake, *Geophys. Res. Lett.*, 22(16), 2309–2312.
- Dziewonski, A., and D. Anderson (1981), Preliminary reference Earth model, *Phys. Earth Planet. Inter.*, 25, 297–356.
- Gilbert, F., and A. M. Dziewonski (1975), An application of normal mode theory to the retrieval of structural parameters and source mechanisms from seismic spectra, *Phil. Trans. R. Soc. Lond.*, 278, 187–269.
- Ni, S., D. Helmberger, and H. Kanamori (2005), Energy radiation from the Sumatra earthquake, *Nature*, 434, 582.
- Okal, E. A., and S. Stein (2009), Observations of ultra-long period normal modes from the 2004 Sumatra-Andaman earthquake, *Phys. Earth Planet. Inter.*, 175, 53–62.
- Park, J., et al. (2005), Earth's free oscillations excited by the 26 December 2004 Sumatra Andaman earthquake, *Science*, 308, 1139–1144.
- Rosat, S., S. Watada, and T. Sato (2007), Geographical variations of the  ${}_0S_0$  normal mode amplitude: predictions and observations after the Sumatra-Andaman earthquake, *Earth Planets Space*, 59, 307–311.
- Simons, M., et al. (2011), The 2011 magnitude 9.0 Tohoku-Oki earthquake: Mosaicking the megathrust from seconds to centuries, *Science*, 332, 1421–1425.
- Stein, S., and E. A. Okal (2007), Ultralong period seismic study of the December 2004 Indian Ocean earthquake and implications for regional tectonics and the subduction process, *Bull. Seismol. Soc. Am.*, 97(1A), S279–S295.
- Stein, S., and M. Wysession (2003), *An Introduction to Seismology, Earthquakes, and Earth Structure*, Blackwell, Malden, Mass., USA.

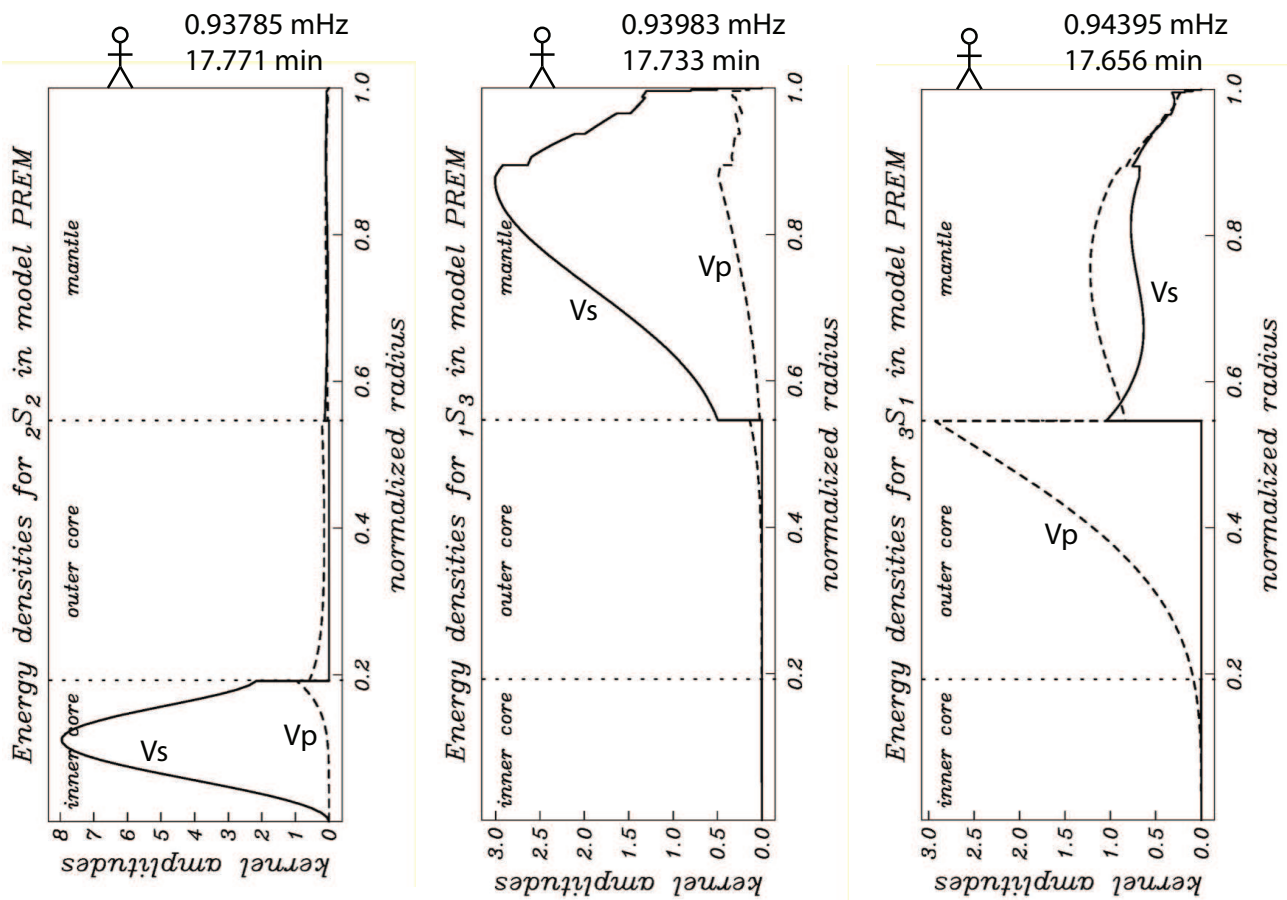


Figure S1: Eigenfunctions of three spheroidal modes near 0.94 mHz:  ${}_2S_2$ ,  ${}_1S_3$ , and  ${}_3S_1$ . These were plotted using the interactive website of Ruedi Widmer-Schnidrig's website (see homework instructions).

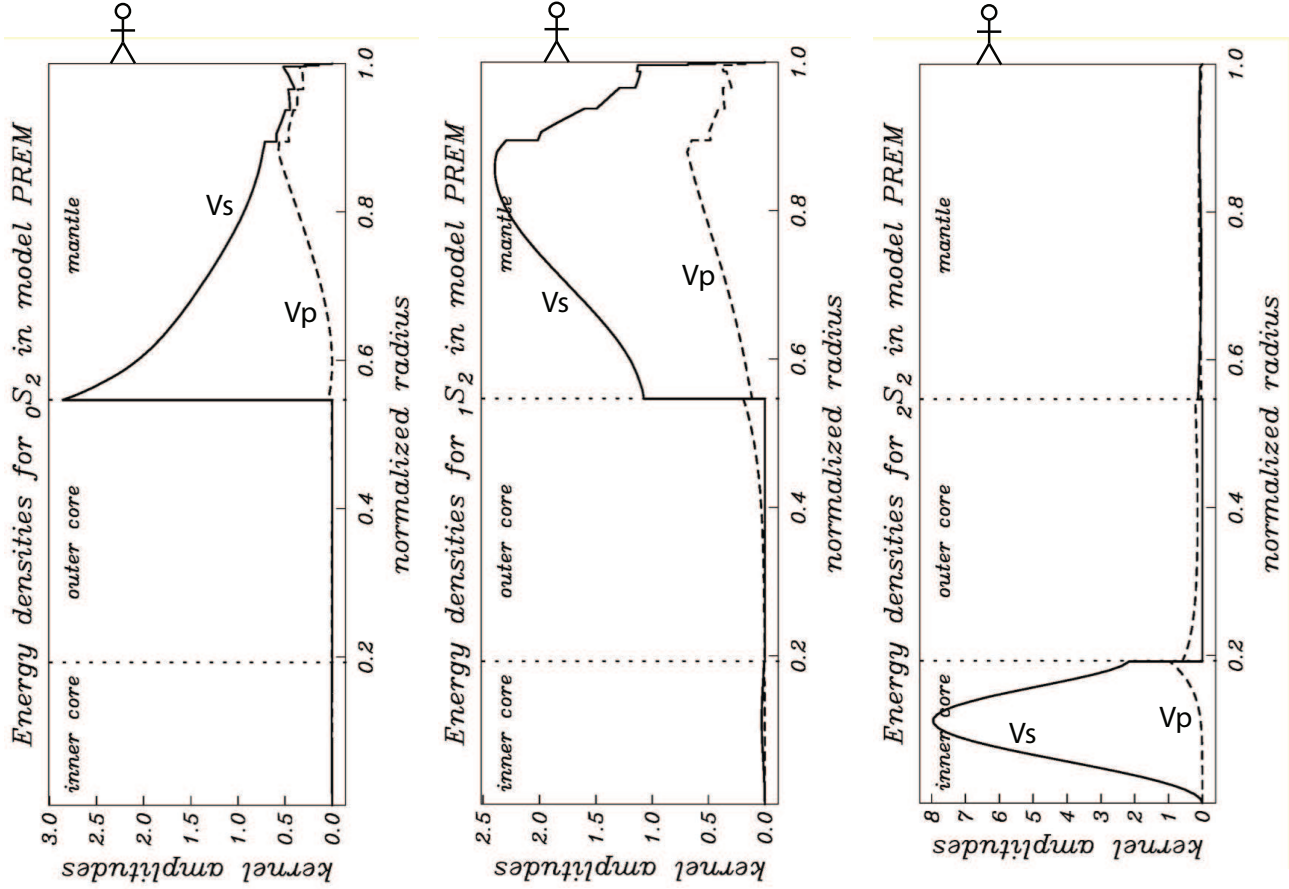


Figure S2: Eigenfunctions of the spheroidal modes  ${}_0S_2$ ,  ${}_1S_2$ , and  ${}_2S_2$  for PREM, plotted using the interactive website of Ruedi Widmer-Schnidrig's websisite (see homework instructions). Notice that  ${}_2S_2$  strongly excites the core but weakly excites the surface, making it difficult to observe. (Here we have  $l = 2$  and  $n = 0, 1, 2$ . For the toroidal shell problem, the index  $n$  was the same as the number of zero crossings of the eigenfunction. Things are more complicated for spheroidal modes and for a more realistic Earth model such as PREM.)

58 points, center at (94.26, 3.09), distance increment 30 deg

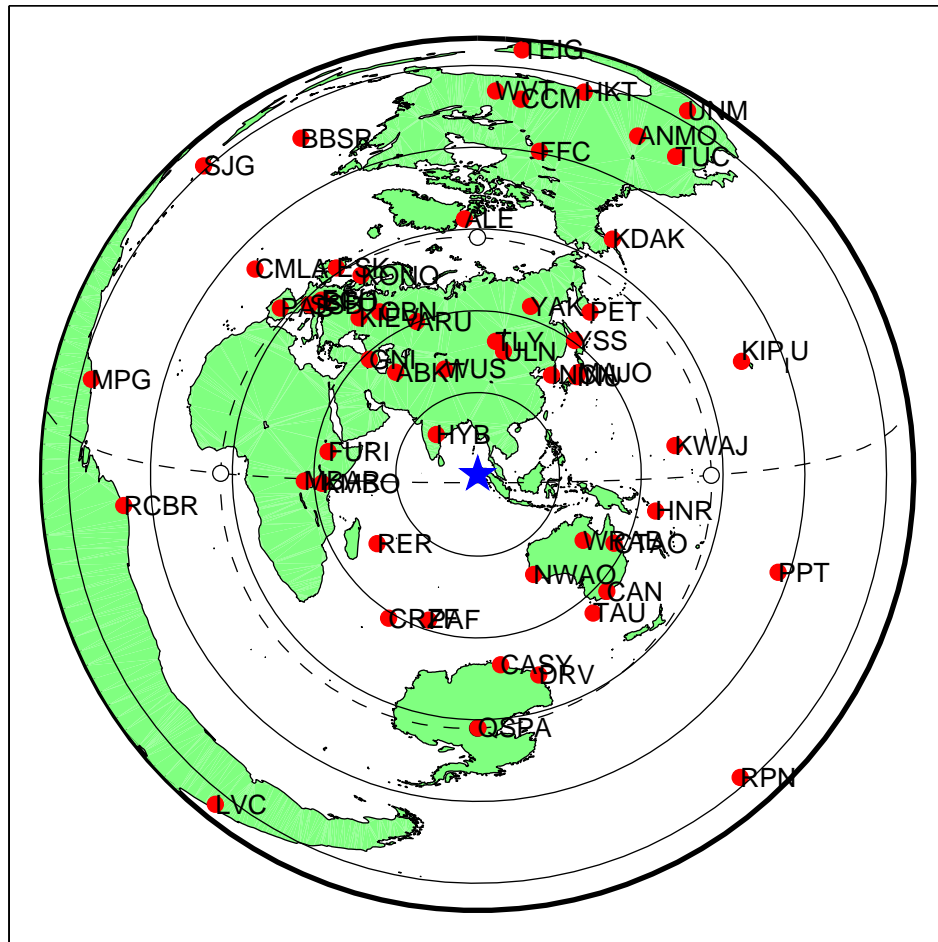


Figure S3: My stations selected for the modes analysis. All stations have an identifiable peak for  ${}_0S_2$  in the frequency spectrum. Spectra were computed using 10-day time series.

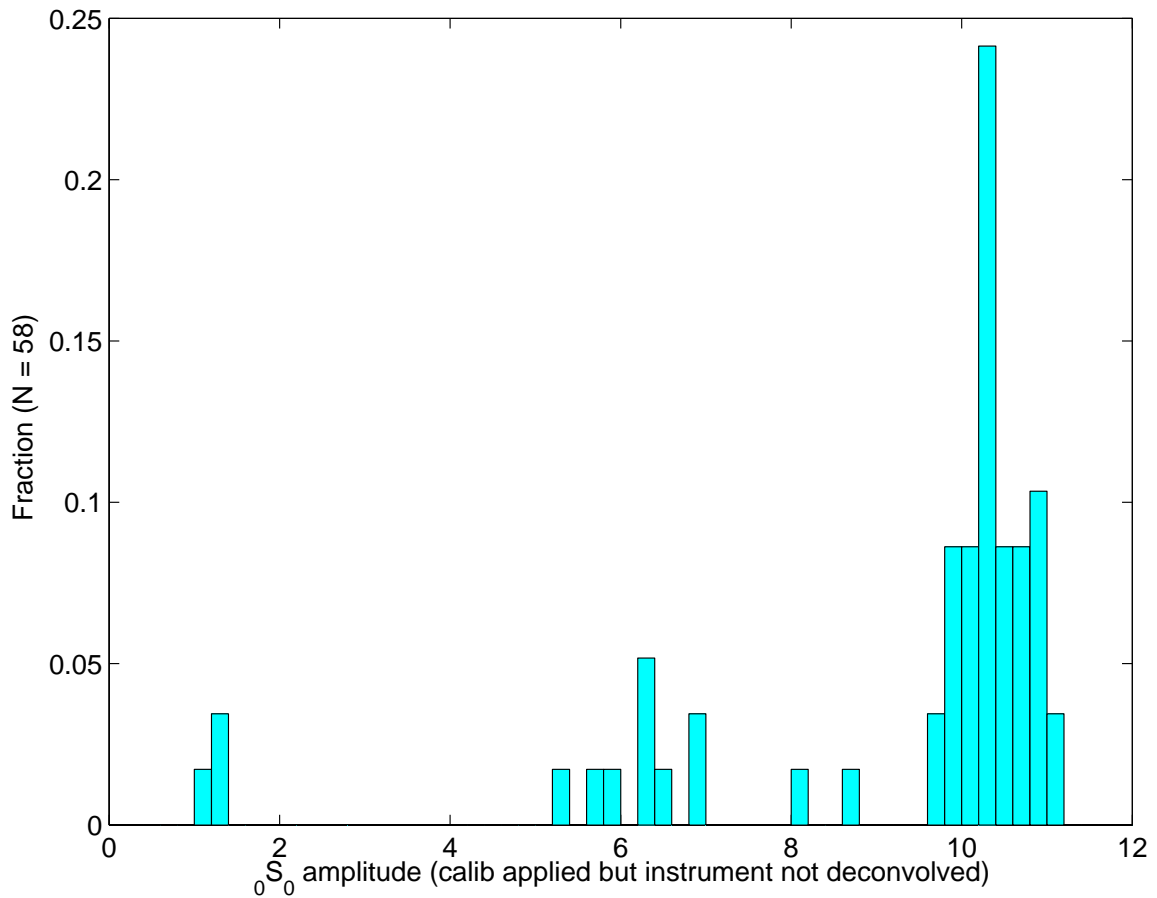


Figure S4: Distribution of amplitude values for the  ${}_0S_0$  peak at all 58 stations. Our analysis uses calibration-applied time series, not instrument-deconvolved time series. In this sense, amplitudes of the peaks are only approximate, but this comparison shows that 90% of the stations have a  ${}_0S_0$  amplitude of about 10.5. See also *Rosat et al.* (2007).

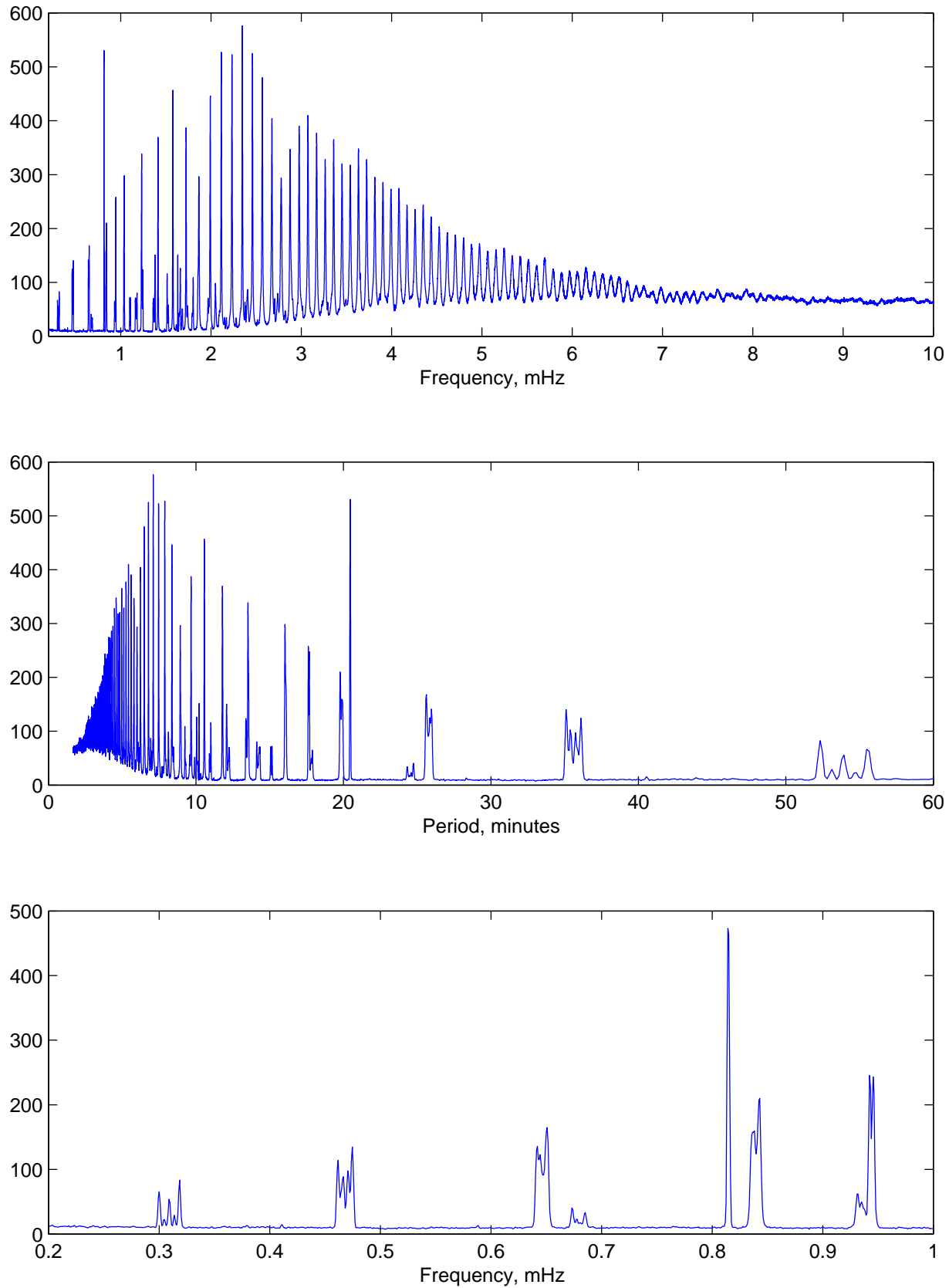


Figure S5: Stacked spectra for all 58 stations. (Top) Spectral excitation of Earth due to the Sumatra earthquake. (Middle) Same as top, but plotted in period (minutes) instead of frequency (mHz). (Bottom) Same as top, but zoomed in on the frequency range of the gravest modes, 0.2 to 1.0 mHz. See Figure S6 for a zoom-in on  ${}_0S_2$ .

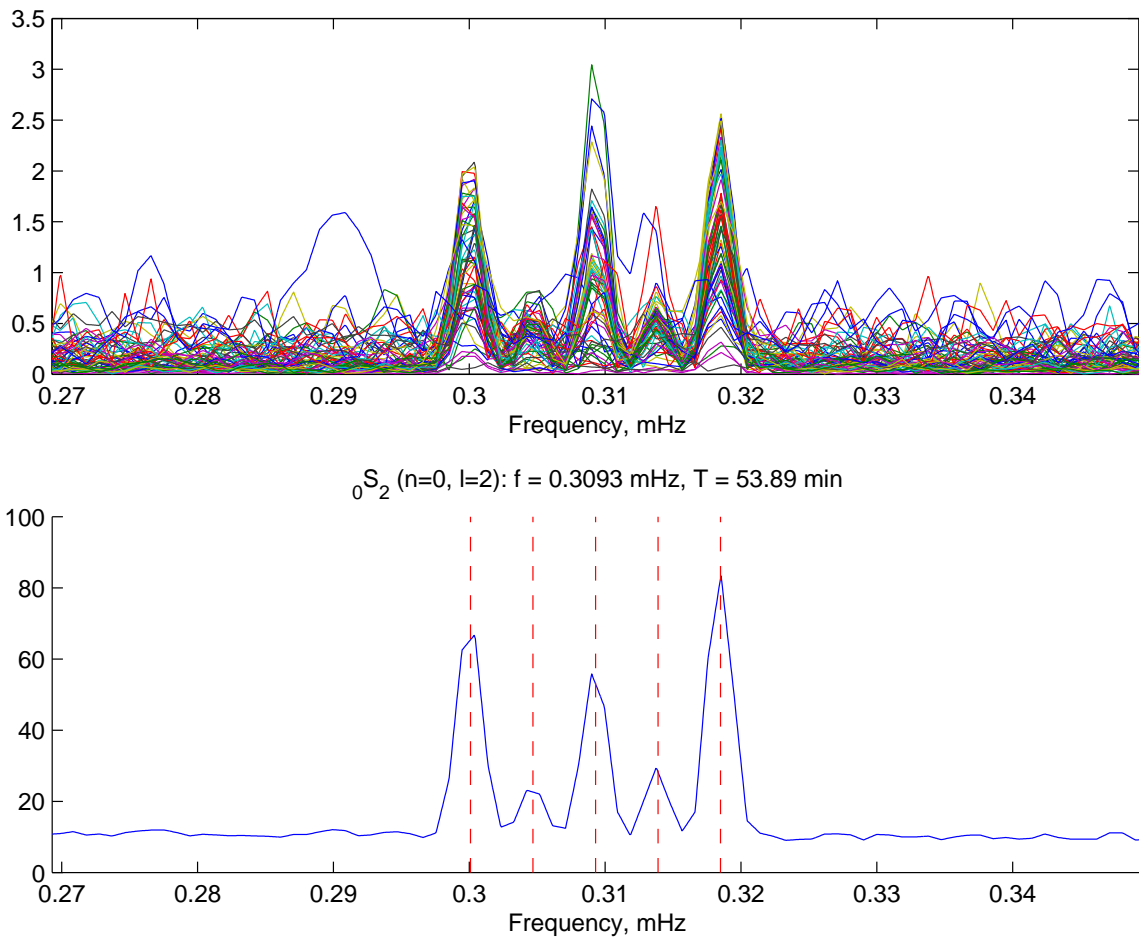


Figure S6: All spectra, plus stack, for  ${}_0S_2$ , the “football mode.” Singlet peaks are split primarily due to the Earth’s rotation.

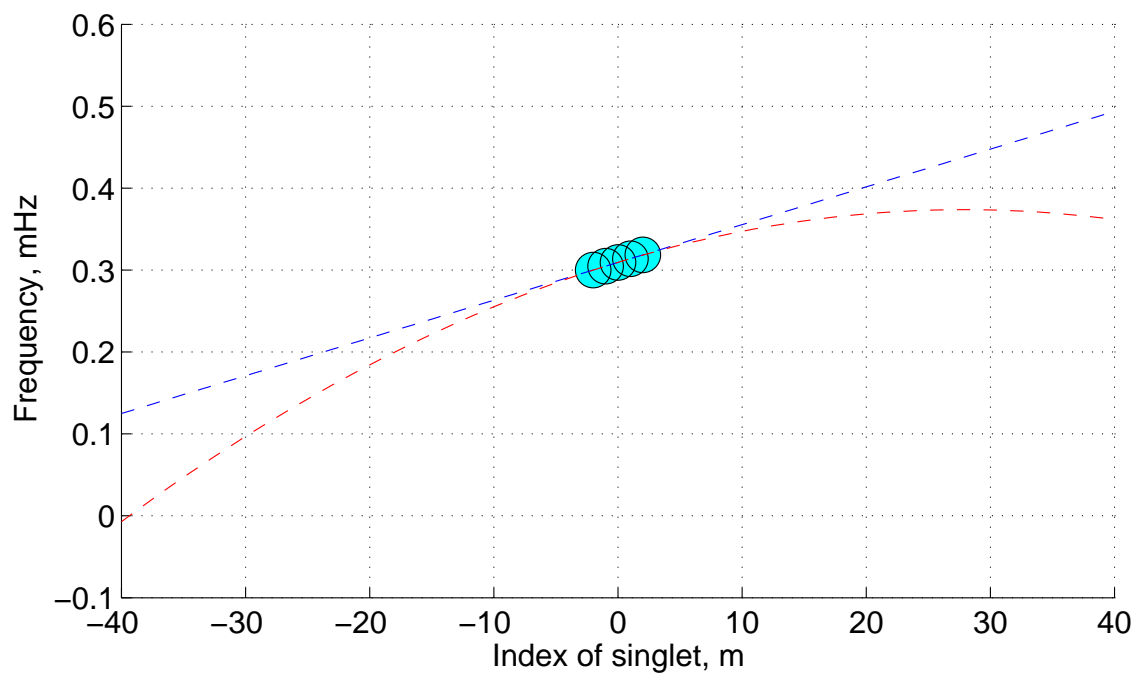
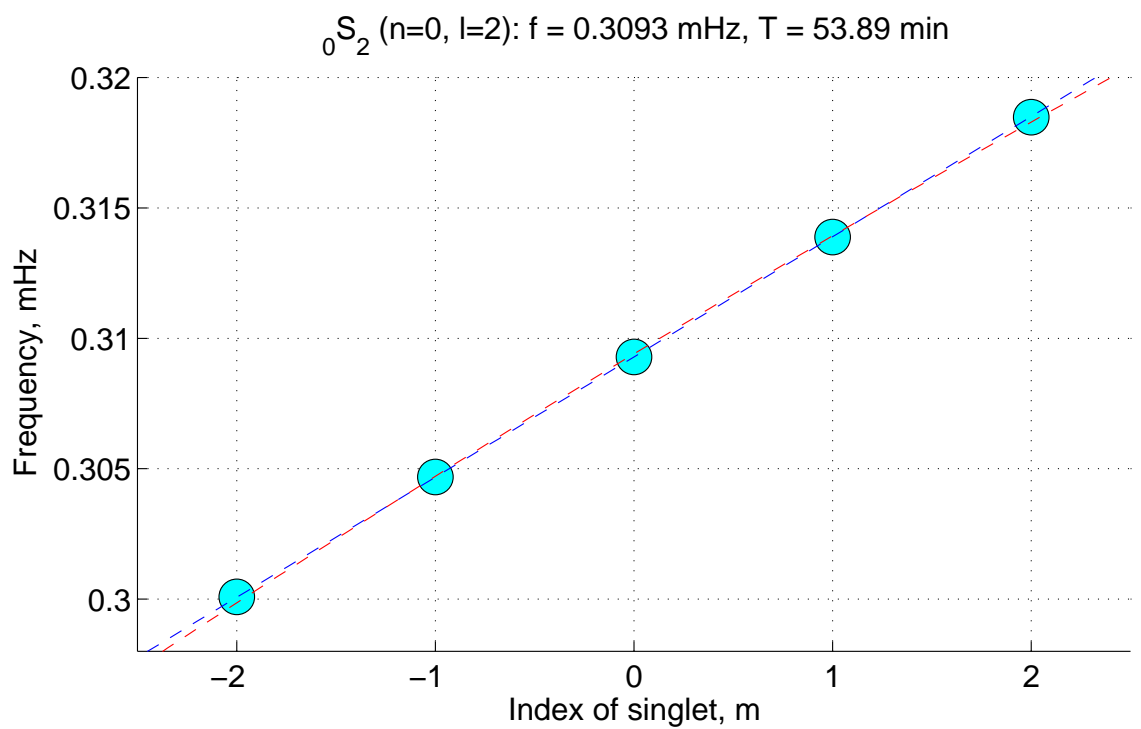


Figure S7: Plot of singlet frequency vs singlet index,  $m$ , for the  $^0S_2$  peaks shown in Figure S6. Dashed lines show theoretical predictions with linear (blue) and quadratic (red) terms.

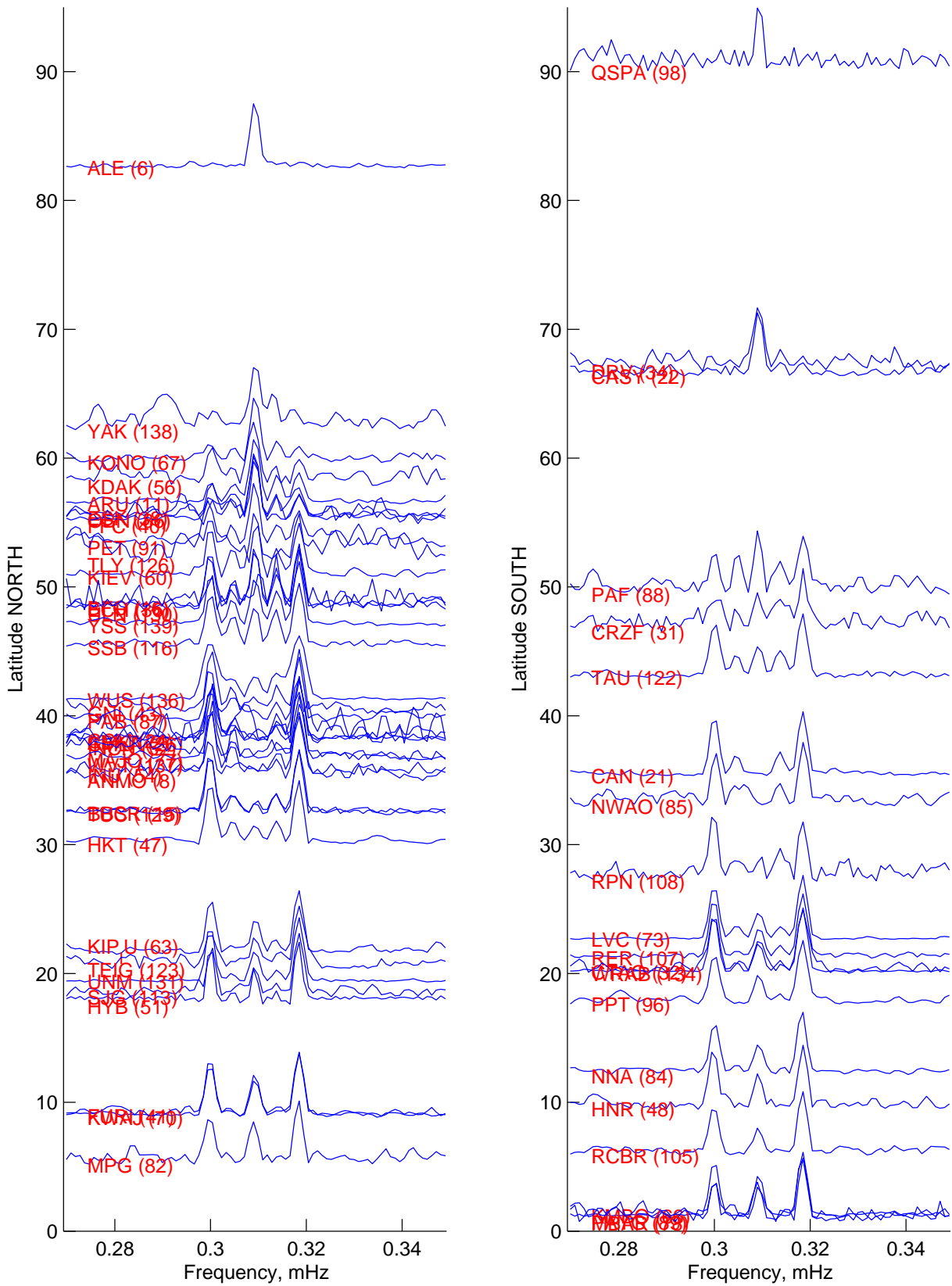


Figure S8: Splitting of  $0S_2$  as a function of latitude. Left column is for the northern hemisphere; right column is for the southern hemisphere. For both plots, the equatorial latitude is at the bottom and the polar latitude is at the top. (The number in parentheses is the index into the 139 available stations.) See also *Stein and Okal (2007)*.

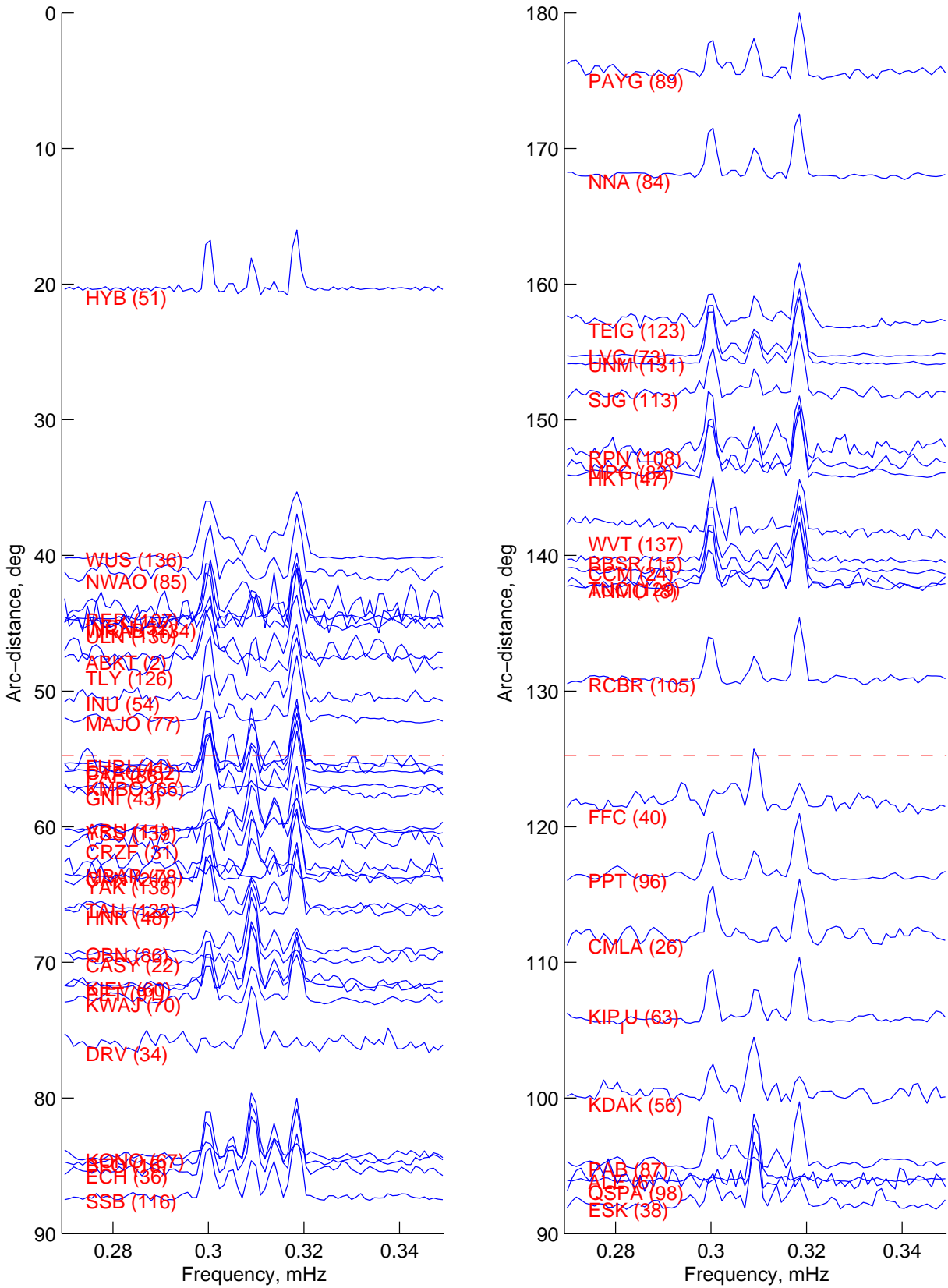


Figure S9: Splitting of  ${}_0S_2$  as a function of source-station arc distance,  $\Delta$ . Left column is for  $0^\circ < \Delta < 90^\circ$  (top to bottom); right column is for  $90^\circ < \Delta < 180^\circ$  (bottom to top). The dashed lines are nodal distances for  ${}_0S_2$  (Eq. S8), where, for a point source in a SNREI model, vertical displacement should be zero. (The number in parentheses is the index into the 139 available stations.)

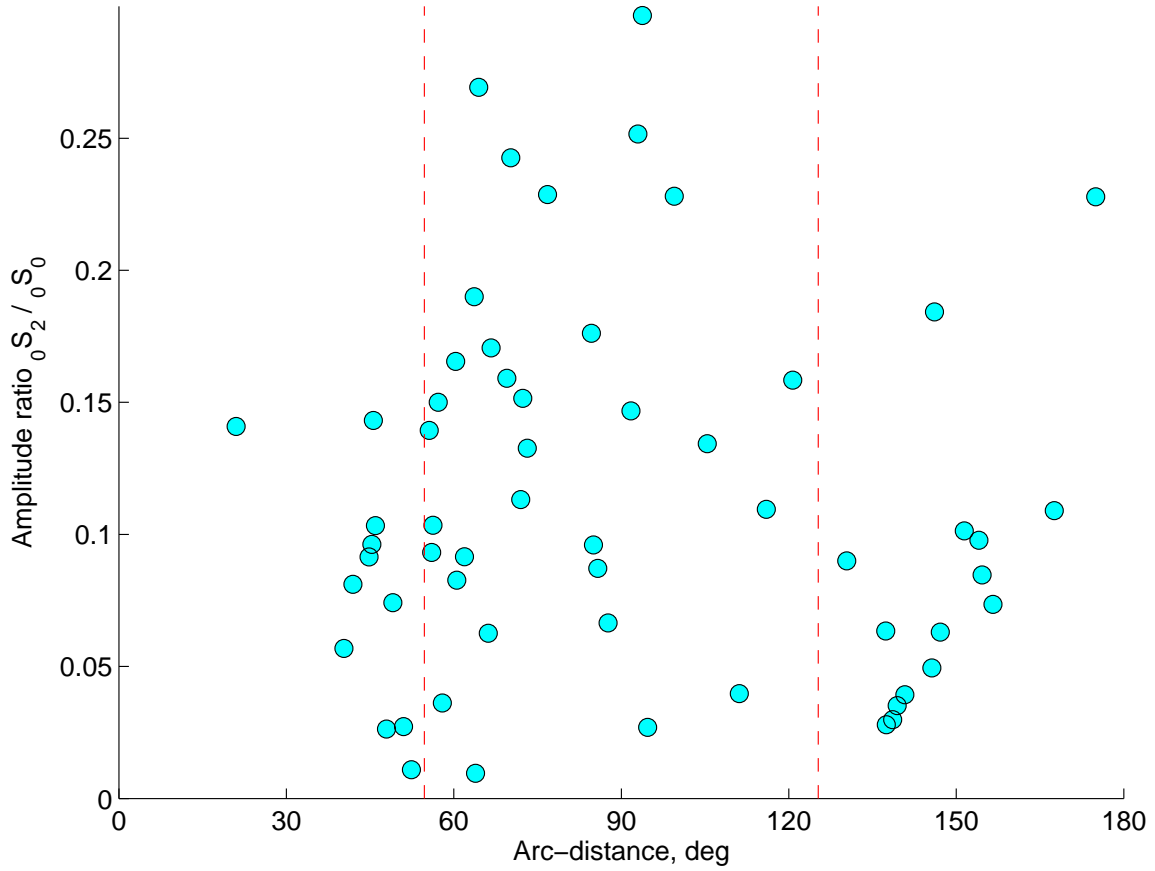


Figure S10: Amplitude of the  $m = 0$  singlet  ${}_0S_2^0$  ( $n = 0, l = 2$ ) as a function of arc distance (see Figure S9). The dashed red lines show the nodal “latitudes” for this mode, at  $54.7^\circ$  and  $125.3^\circ$  from the epicenter (Eq. S8). The amplitude is normalized by the  ${}_0S_0$  peak in order to diminish the effects of not removing the instrument response. A more detailed analysis is needed in order to test the hypothesis that the excitation of  ${}_0S_2$  is weakest near the nodal lines, as one would expect for a SNREI Earth model.

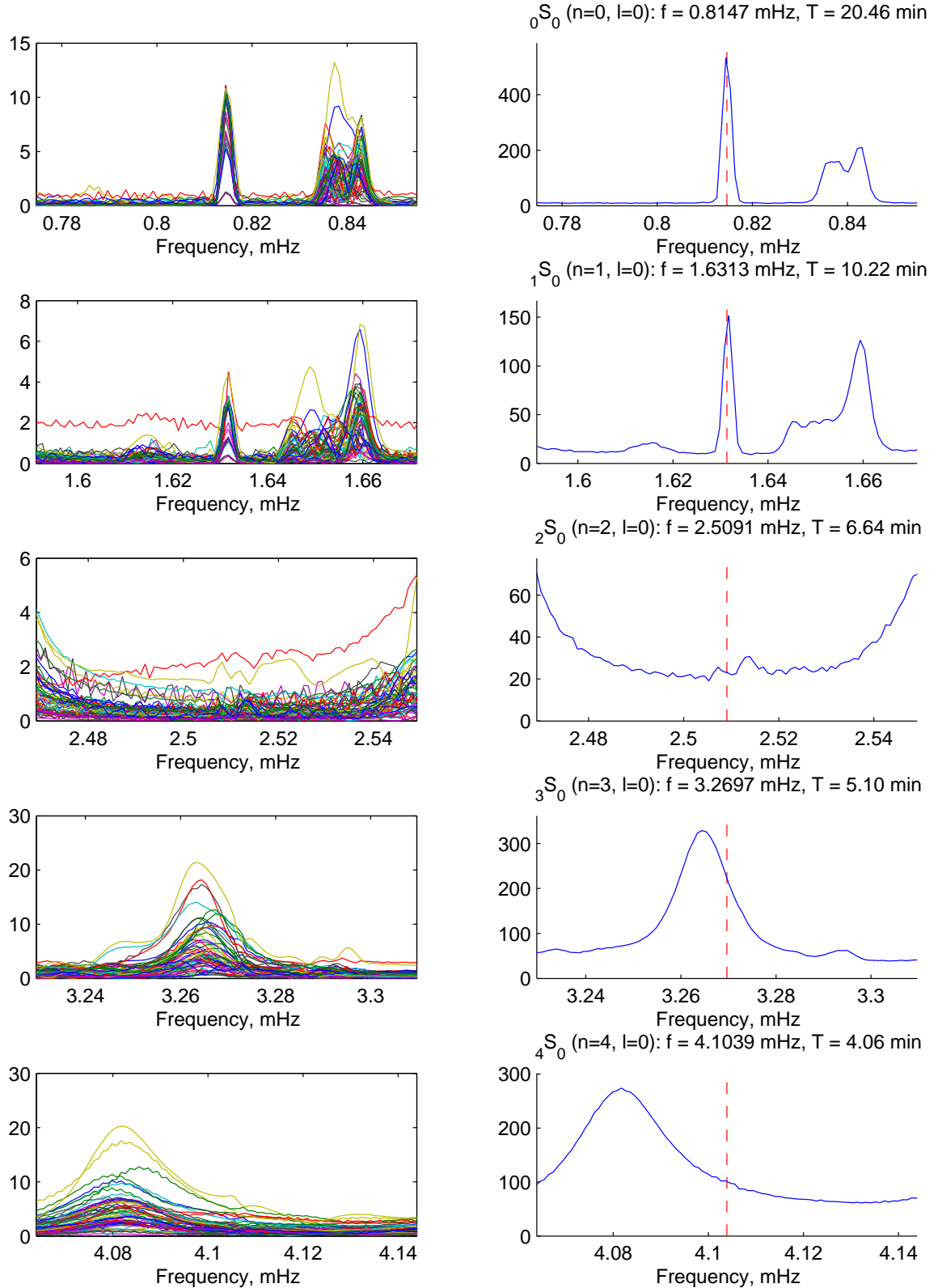


Figure S11: Searching for radial modes in the Sumatra spectrum:  ${}_0S_0$ ,  ${}_1S_0$ ,  ${}_2S_0$ ,  ${}_3S_0$ , and  ${}_4S_0$ . Only  ${}_0S_0$  and  ${}_1S_0$  are definitively visible. Probably  ${}_2S_0$  is the smaller of the two peaks visible (2.5091 mHz), the other being  ${}_7S_2$  (2.5165 mHz). The two broad peaks are fundamental mode Rayleigh waves:  ${}_0S_{24}$  (not  ${}_3S_0$ ) and  ${}_0S_{33}$  (not  ${}_4S_0$ ).

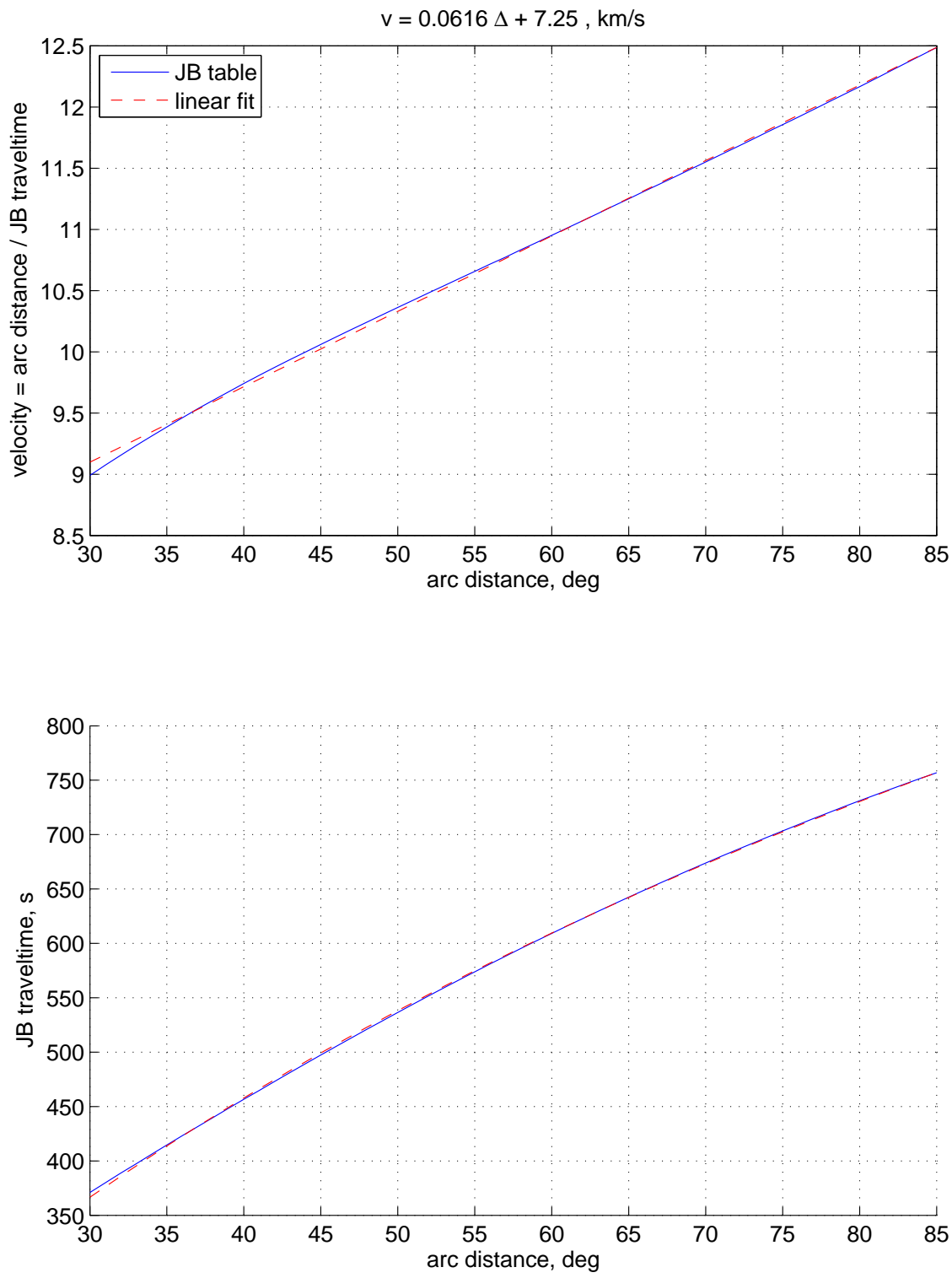


Figure S12: P wave traveltimes from Jeffreys-Bullen tables. The calculations are based on a source depth of 10 km. (a) Apparent P velocity as a function epicentral distances, based on the Jeffreys-Bullen travel time tables. The mean velocity over the epicentral distance range  $30^\circ < \Delta < 85^\circ$  is 10.8 km/s, which would provide a very rough approximation for the P wave velocity for all stations. (b) Linear fit transformed to traveltime:  $P_t = \Delta_{\text{km}} / (0.616\Delta + 7.25)$ .

variable time shifts: reference time is 2004–12–26 00:58:50; TLY max 4.29e+02 nm / sec at t = 401.5 s  
 BHZ BHZ\_00 BHZ\_20 [ nm / sec, ---] event M122604A (2004–12–26, M9.0, 95.8, 3.3, z = 10.0 km)  
 50 / 50 seismograms (50 stations) ordered by azimuth, norm --> max(abs(d\_i))

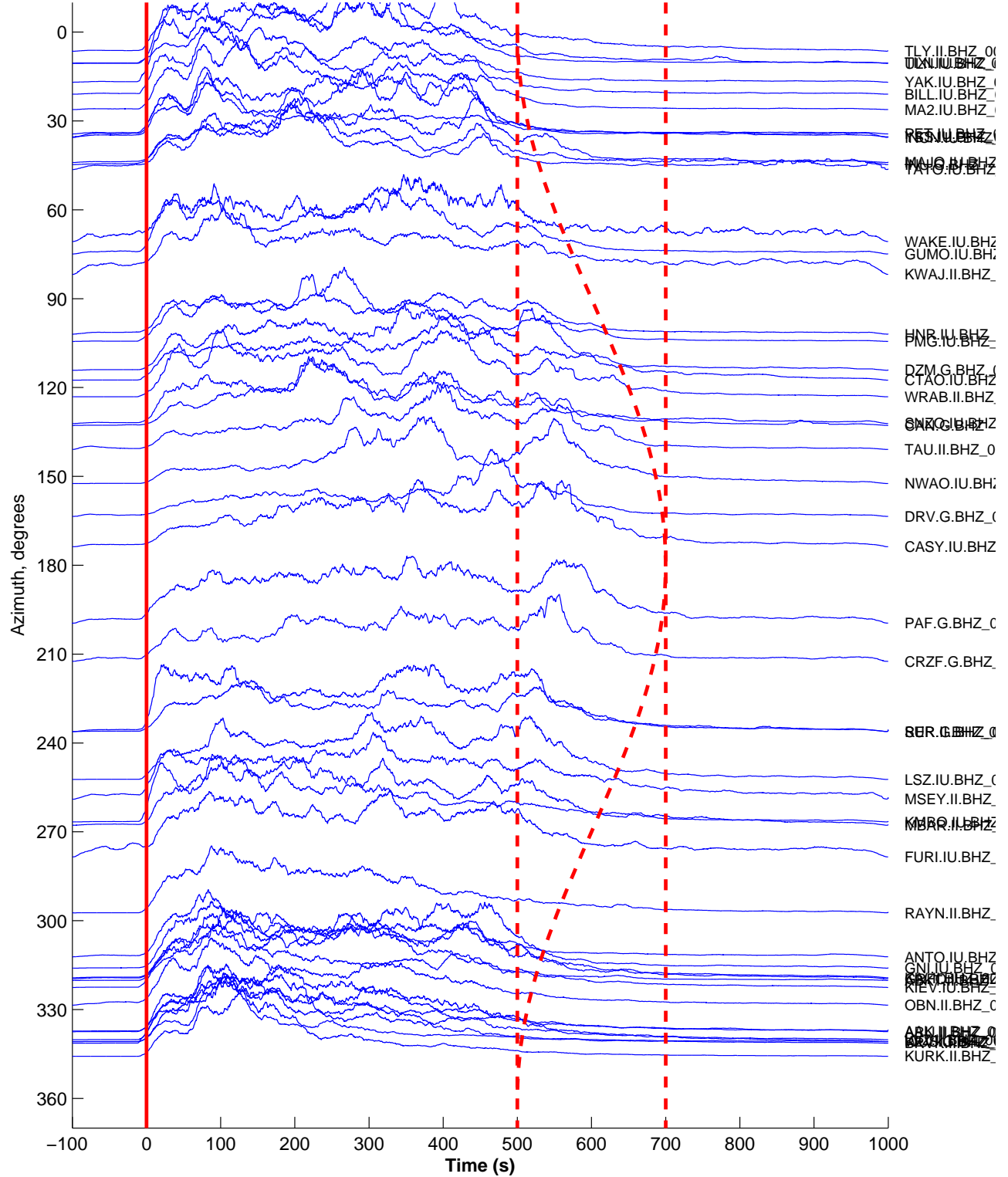


Figure S13: Reproducing the analysis of Ni et al. (2005): azimuthal record section of the smoothed envelopes of high-frequency (2–4 Hz) vertical component velocity seismograms, aligned on the predicted P onset ( $t = 0$ ). All stations with epicentral distance  $30^\circ < \Delta < 85^\circ$  are used. The duration of signal as a function of azimuth can be approximated by Eq. S24 with  $T_{\min} = 500$  s,  $T_{\max} = 700$  s, and  $\alpha_0 = 0^\circ$ .

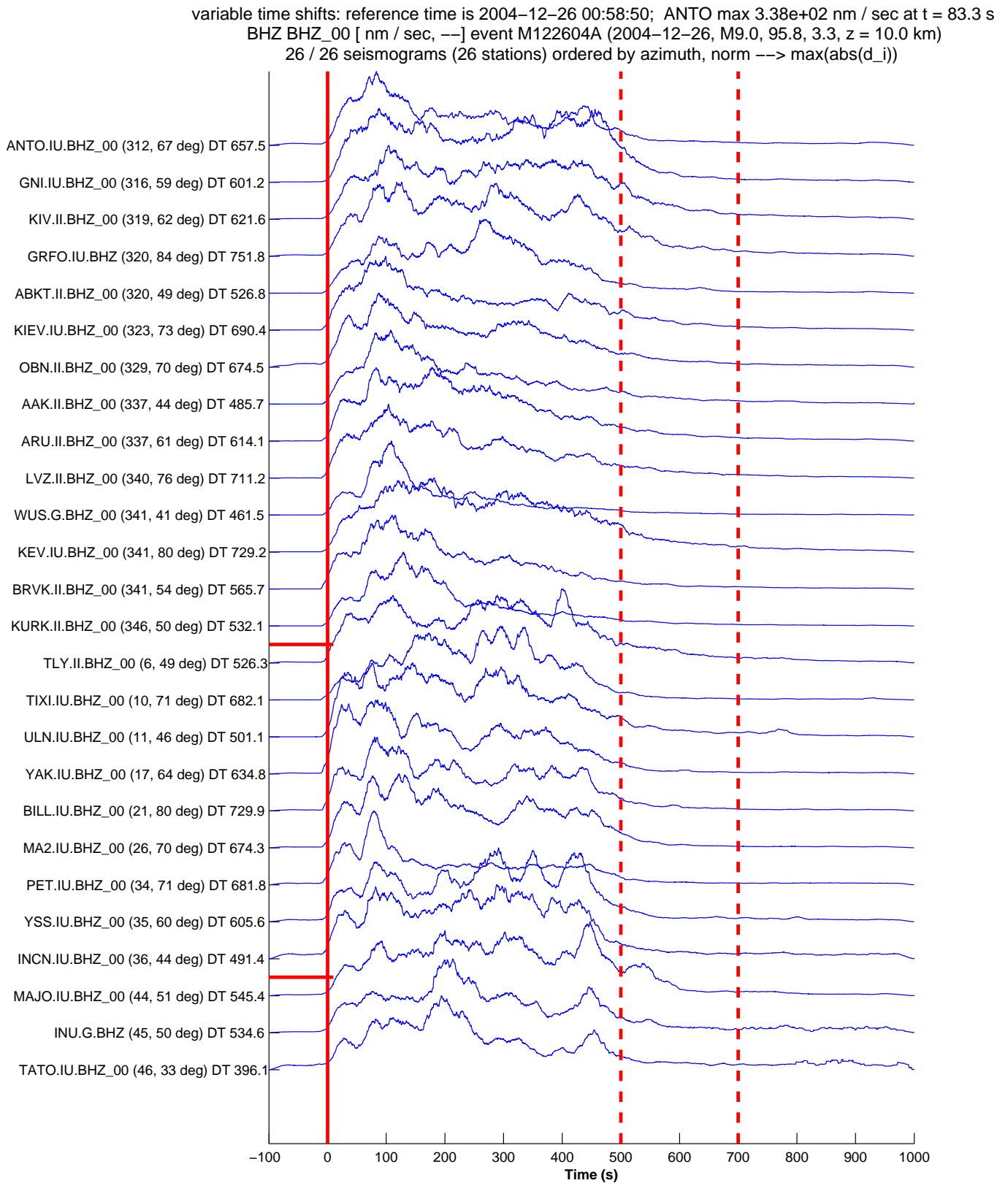


Figure S14: All stations in Figure S13 within  $50^\circ$  of the direction of rupture,  $\alpha_0 = 0^\circ$ . Compare with the stations in direction opposite of rupture in Figure S15.

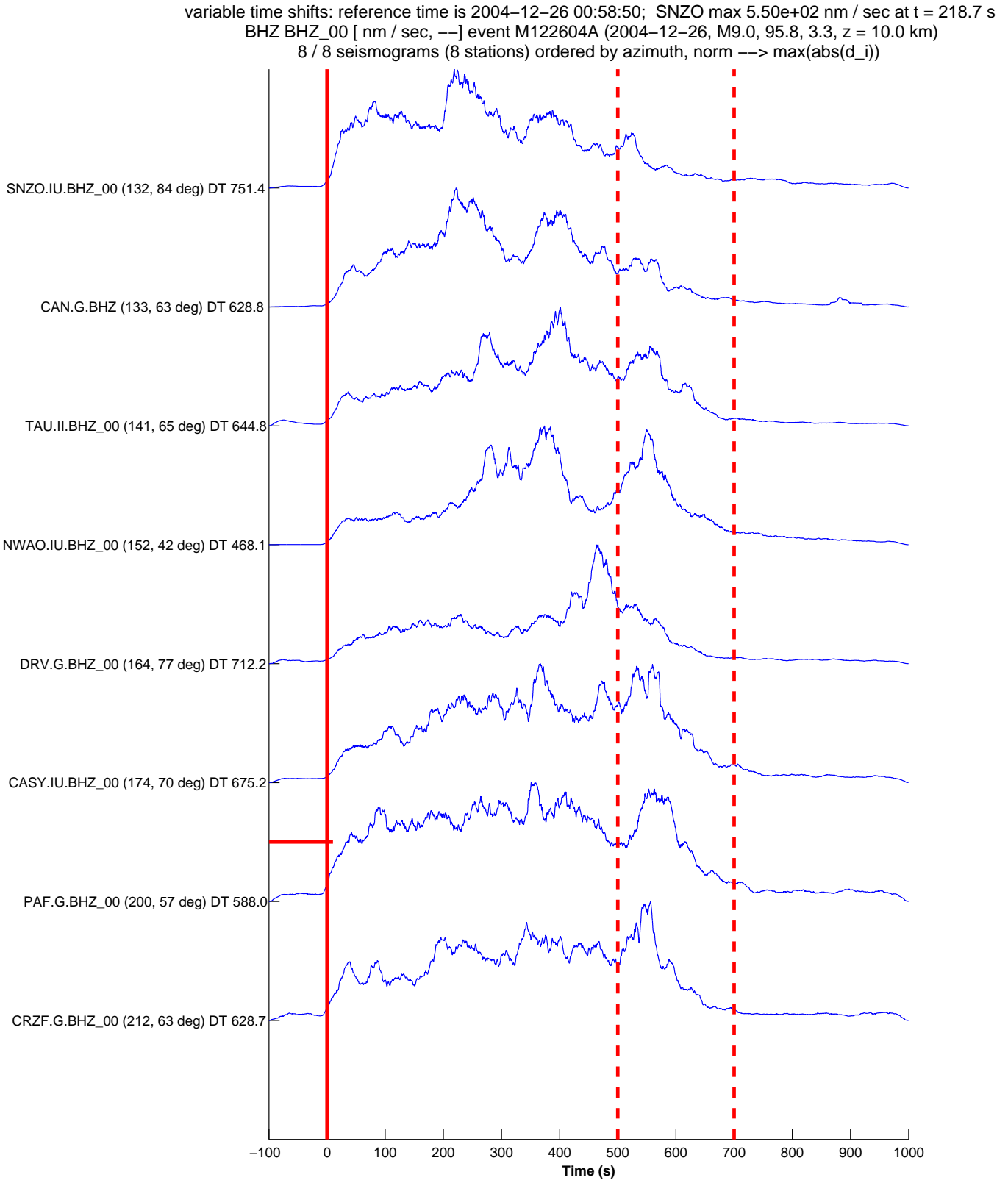


Figure S15: All stations in Figure S13 within  $50^\circ$  of the direction *opposite* to rupture,  $\alpha_0 + 180^\circ = 180^\circ$ . Compare with the stations in direction of rupture in Figure S14. Note that CAN, from the previous homework, is in this record section.

33 points, center at (94.26, 3.09), distance increment 30 deg

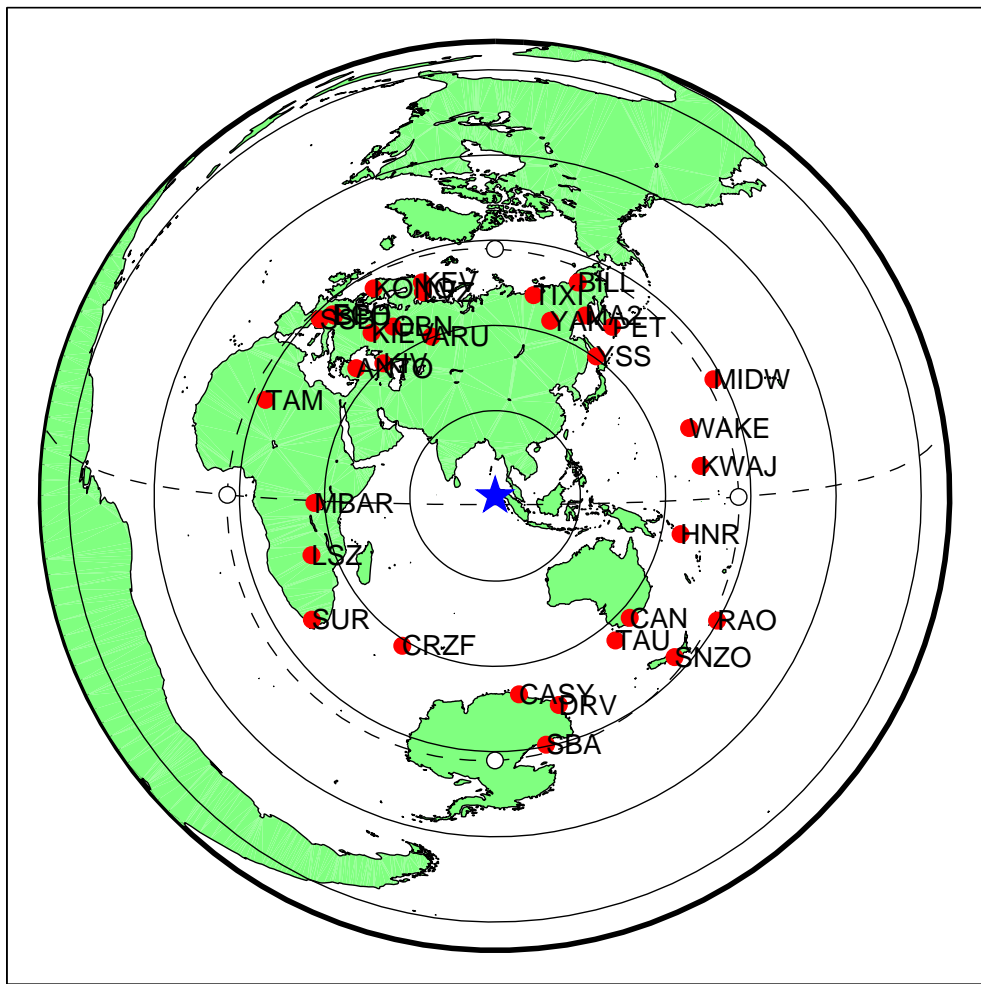


Figure S16: Map of stations used in the long-period directivity analysis in Figures S17–S22. Station epicentral distances are  $60^\circ < \Delta < 90^\circ$ .

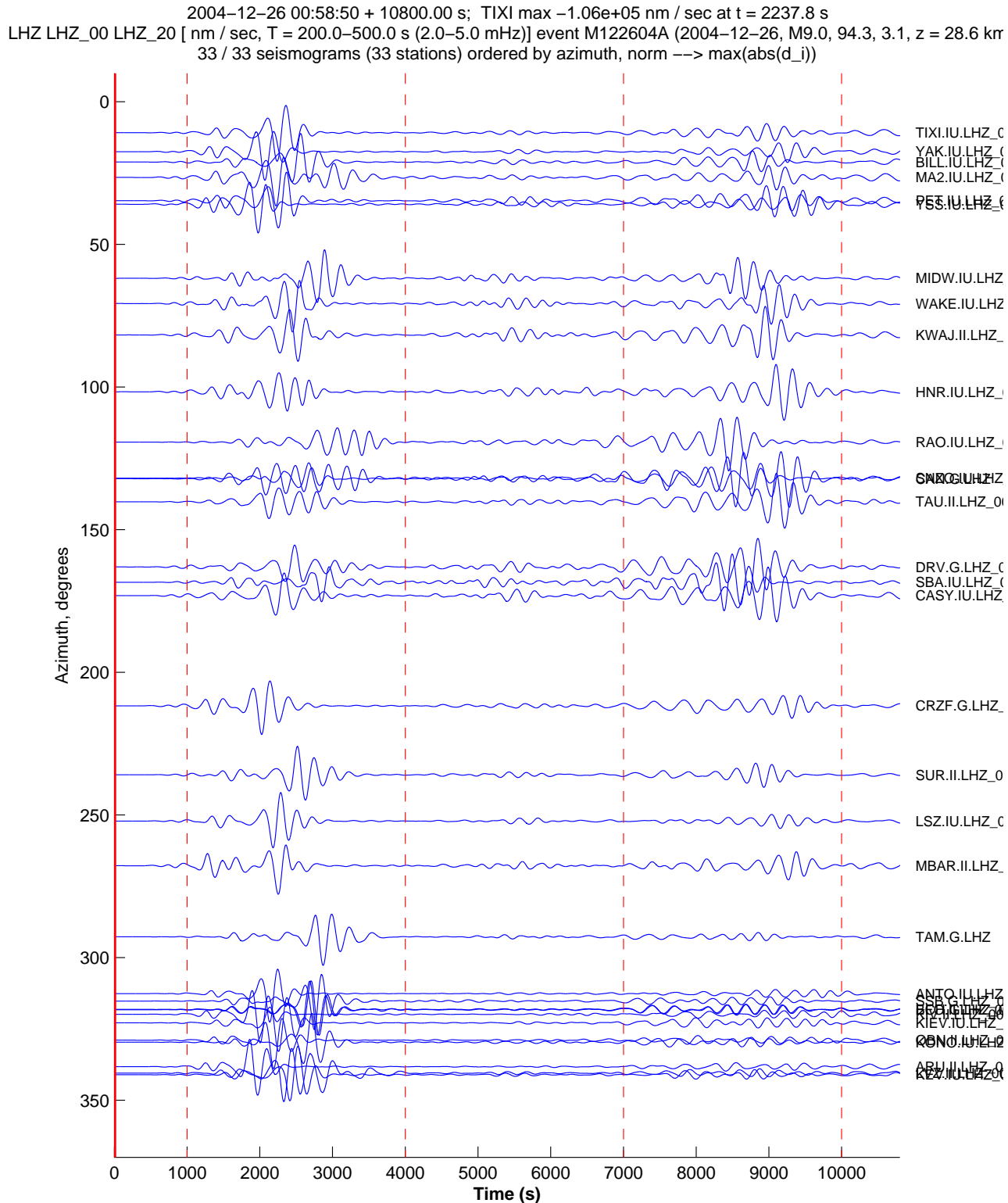


Figure S17: Azimuthal record section of vertical component velocity seismograms, filtered 200–500 s.

2004-12-26 00:58:50 + 10800.00 s; TIXI max 1.11e+05 nm / sec at t = 2278.8 s  
 LHZ LHZ\_00 LHZ\_20 [ nm / sec, --] event M122604A (2004-12-26, M9.0, 94.3, 3.1, z = 28.6 km)  
 33 / 33 seismograms (33 stations) ordered by azimuth, norm --> max(abs(d\_i))

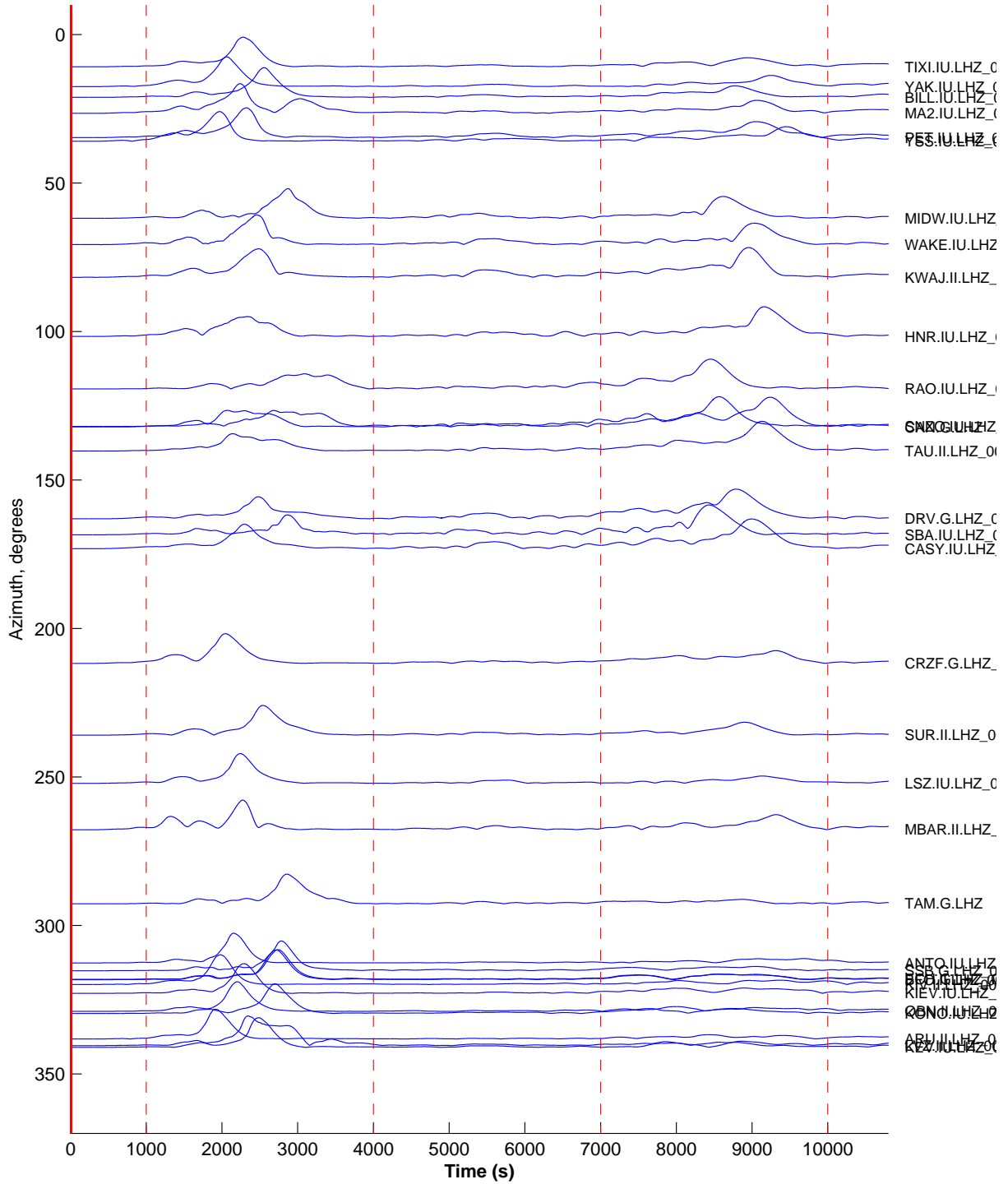


Figure S18: Envelopes of seismograms in Figure S17, computed using a Hilbert transform (hilbert).

R1/R2 amplitude ratio as a function of station azimuth ( $T = 200\text{--}500$  s)  
 best-fitting function provides estimate of  $\alpha_0 = 310$  deg  
 markers colored by station distance

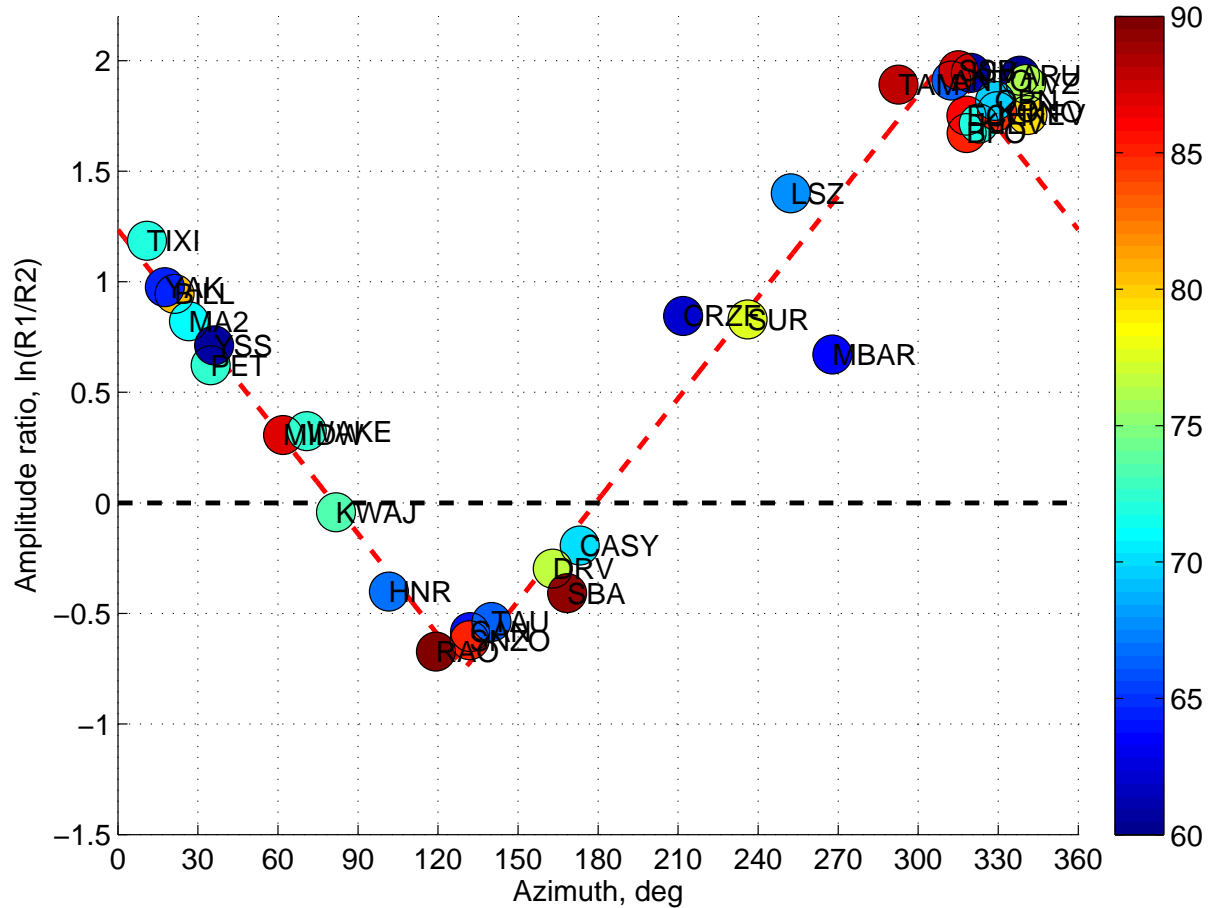


Figure S19: R1/R2 amplitude ratio as a function of station azimuth. Largest R1/R2 ratios occur in the rupture direction, estimated here to be  $\alpha_0 = 310^\circ$ . Smallest R1/R2 ratios occur in the opposite direction ( $\alpha = 140^\circ$ ). The seismograms have *not* had their instrument responses deconvolved, which really ought to be done for these long periods. However, deconvolution does not change the overall pattern seen here.

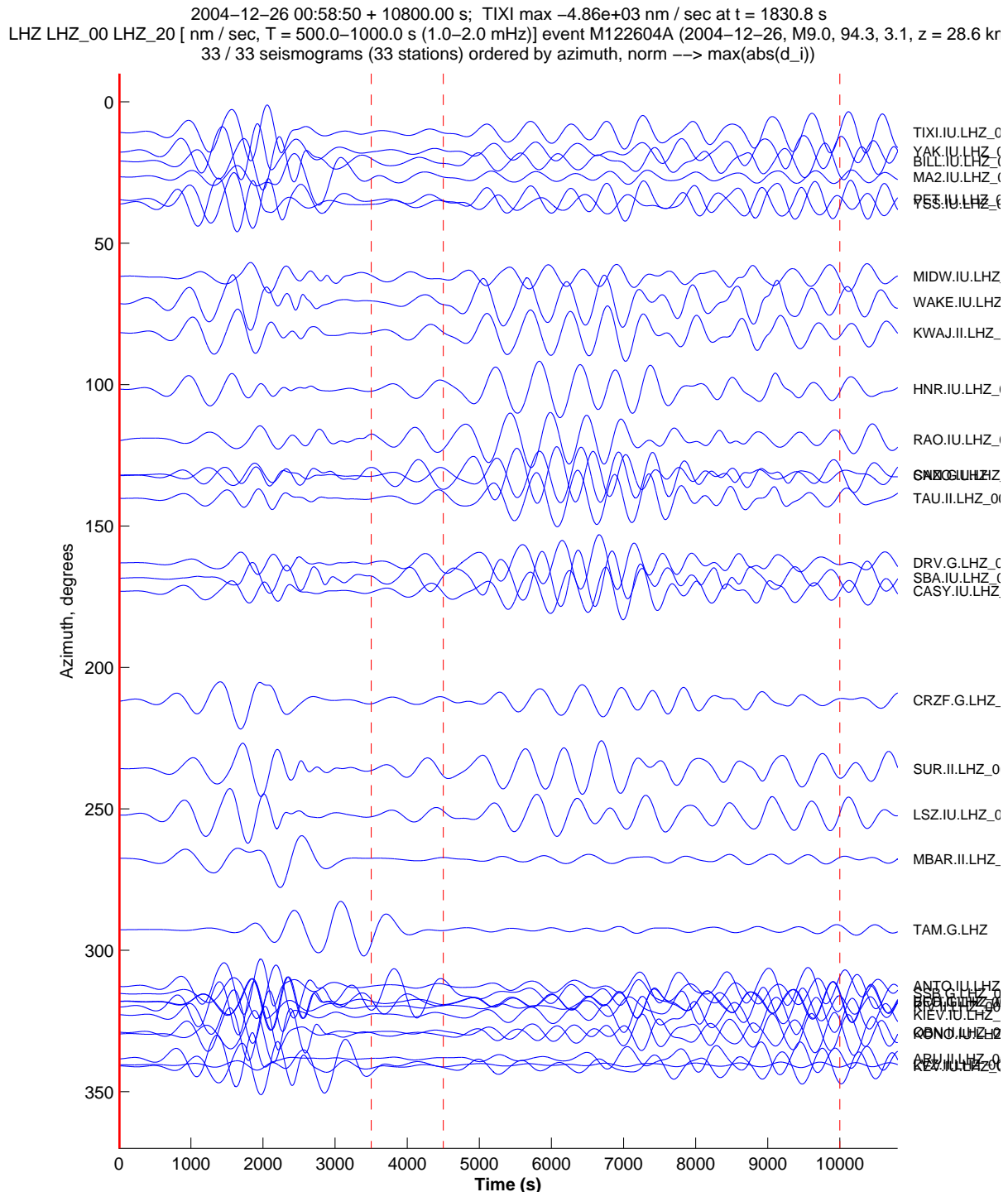


Figure S20: Same as Figure S17, but with 500–1000 s.

2004-12-26 00:58:50 + 10800.00 s; TIXI max 4.93e+03 nm / sec at t = 1909.8 s  
 LHZ LHZ\_00 LHZ\_20 [ nm / sec, ---] event M122604A (2004-12-26, M9.0, 94.3, 3.1, z = 28.6 km)  
 33 / 33 seismograms (33 stations) ordered by azimuth, norm ---> max(abs(d\_i))

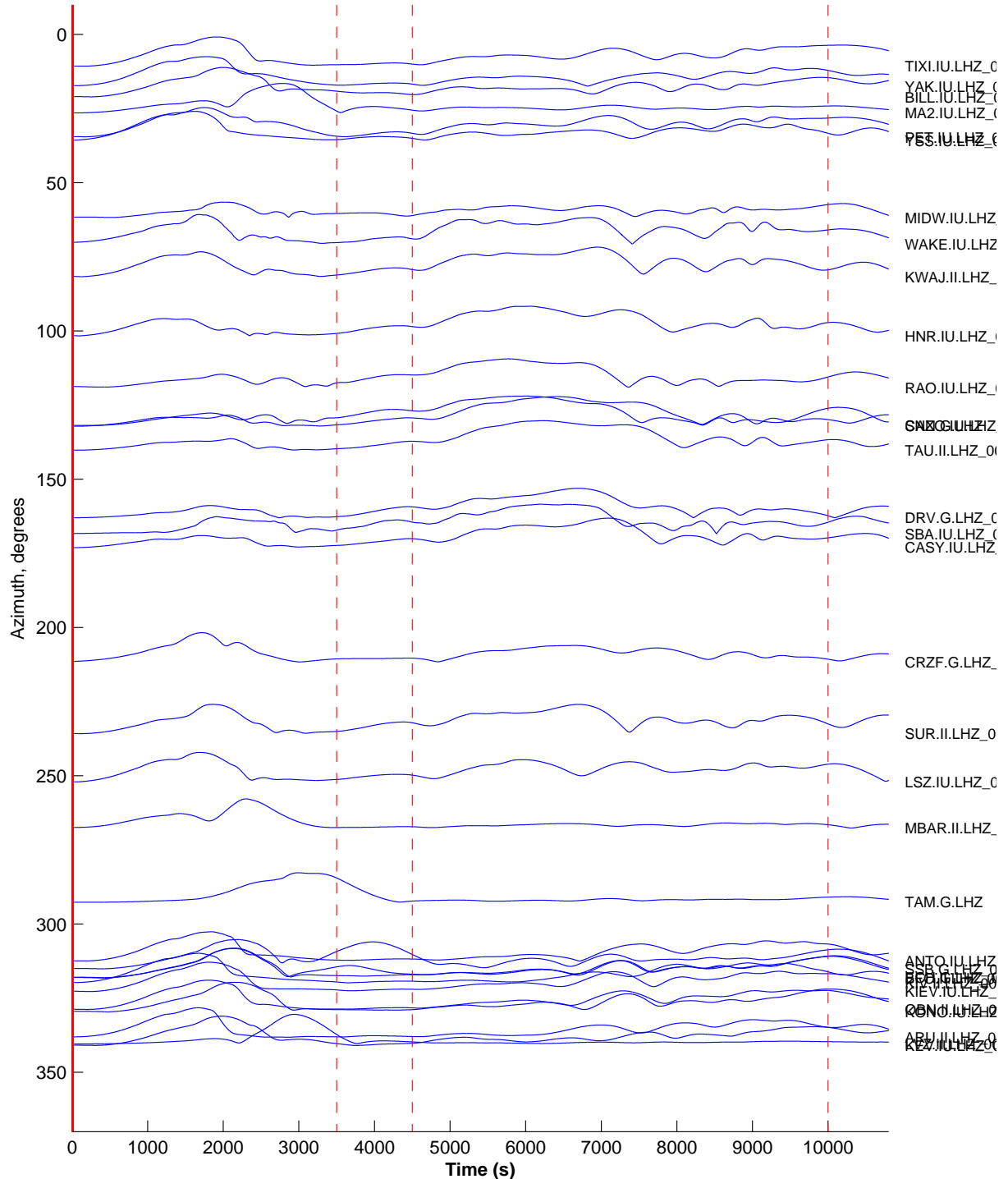


Figure S21: Same as Figure S18, but with 500–1000 s.

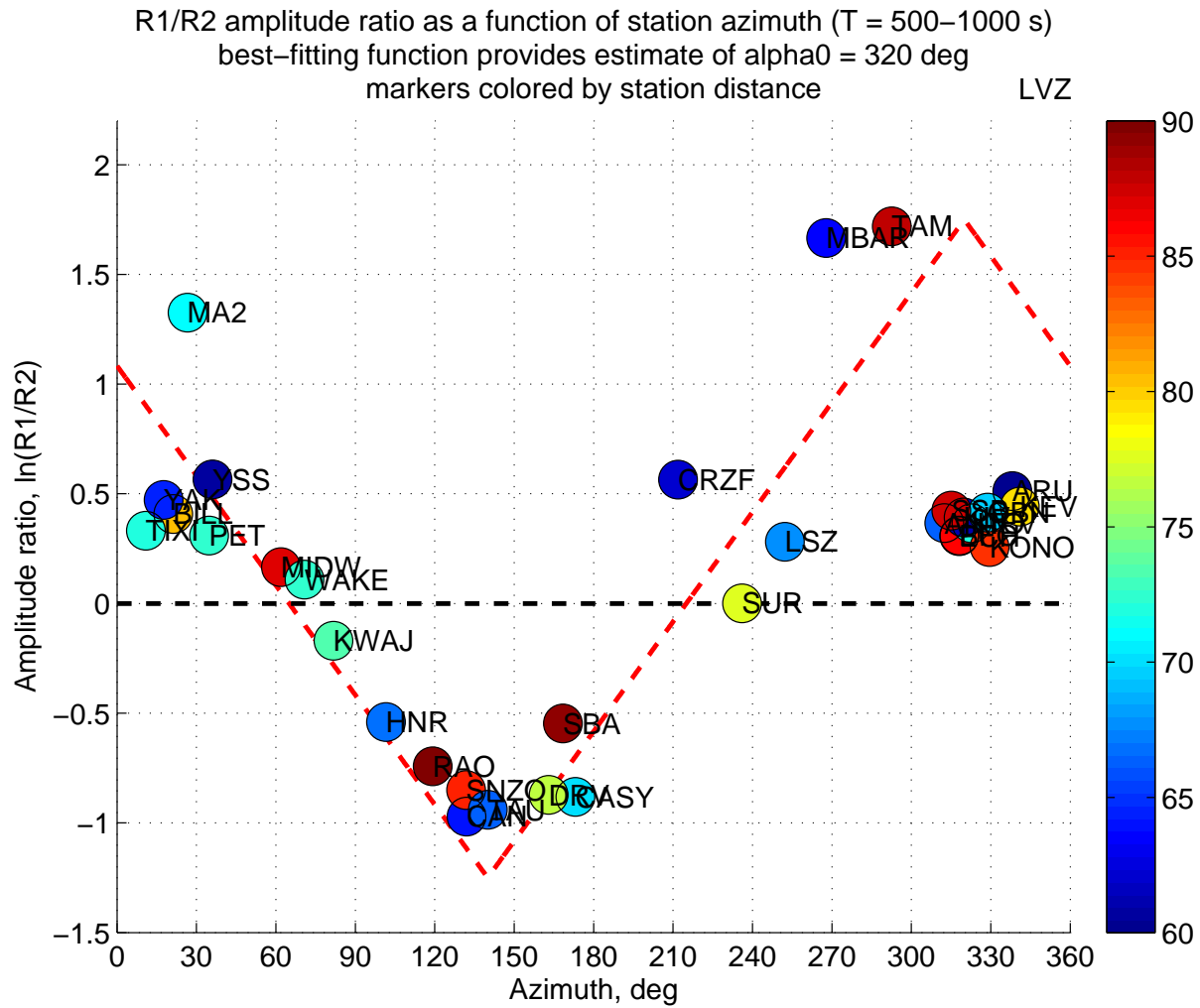


Figure S22: Same as Figure S19, but with  $500\text{--}1000$  s. Here the triangle function implies a rupture direction of  $\alpha_0 = 320^\circ$ .

8 points, center at (94.26, 3.09), distance increment 30 deg

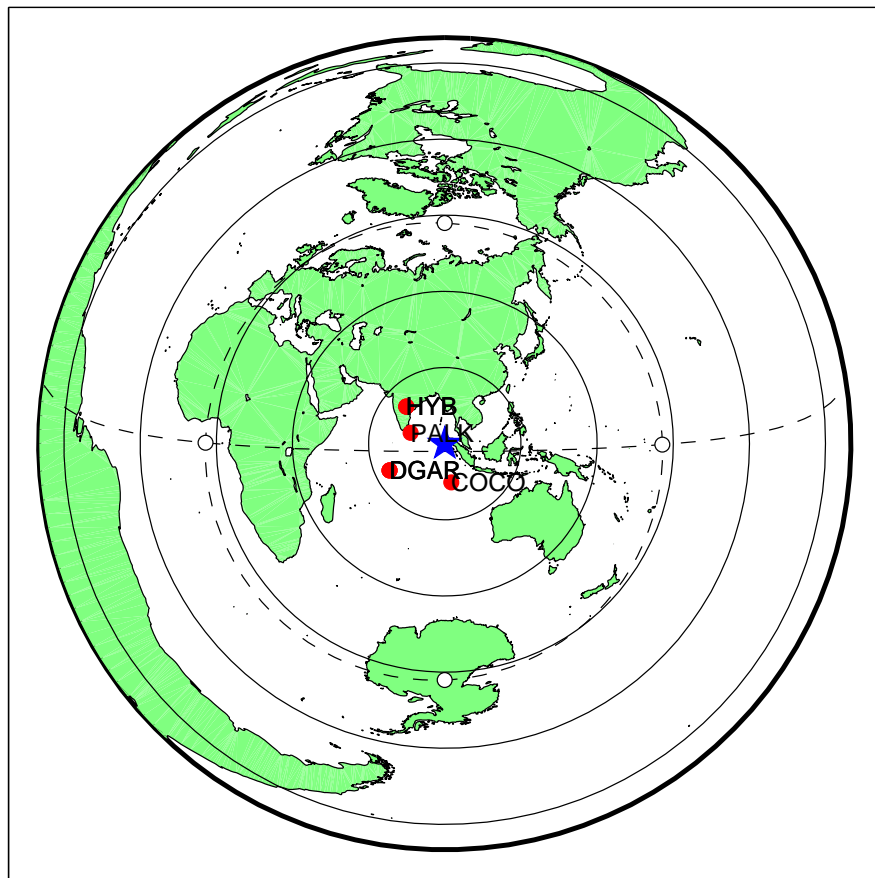


Figure S23: Near-source stations used in Figures S25 and S24.

variable time shifts: reference time is 2004-12-26 00:58:50; PALK max -2.79e+07 nm at t = 330.5 s  
LHE LHE\_10 LHN LHN\_10 LHZ LHZ\_00 LHZ\_10 [ nm, T = 50.0–500.0 s (2.0–20.0 mHz) ] event M122604A (2004-12-26, M9.0, 9-  
8 / 8 seismograms (4 stations) ordered by distance, norm --> max(abs(d\_i))

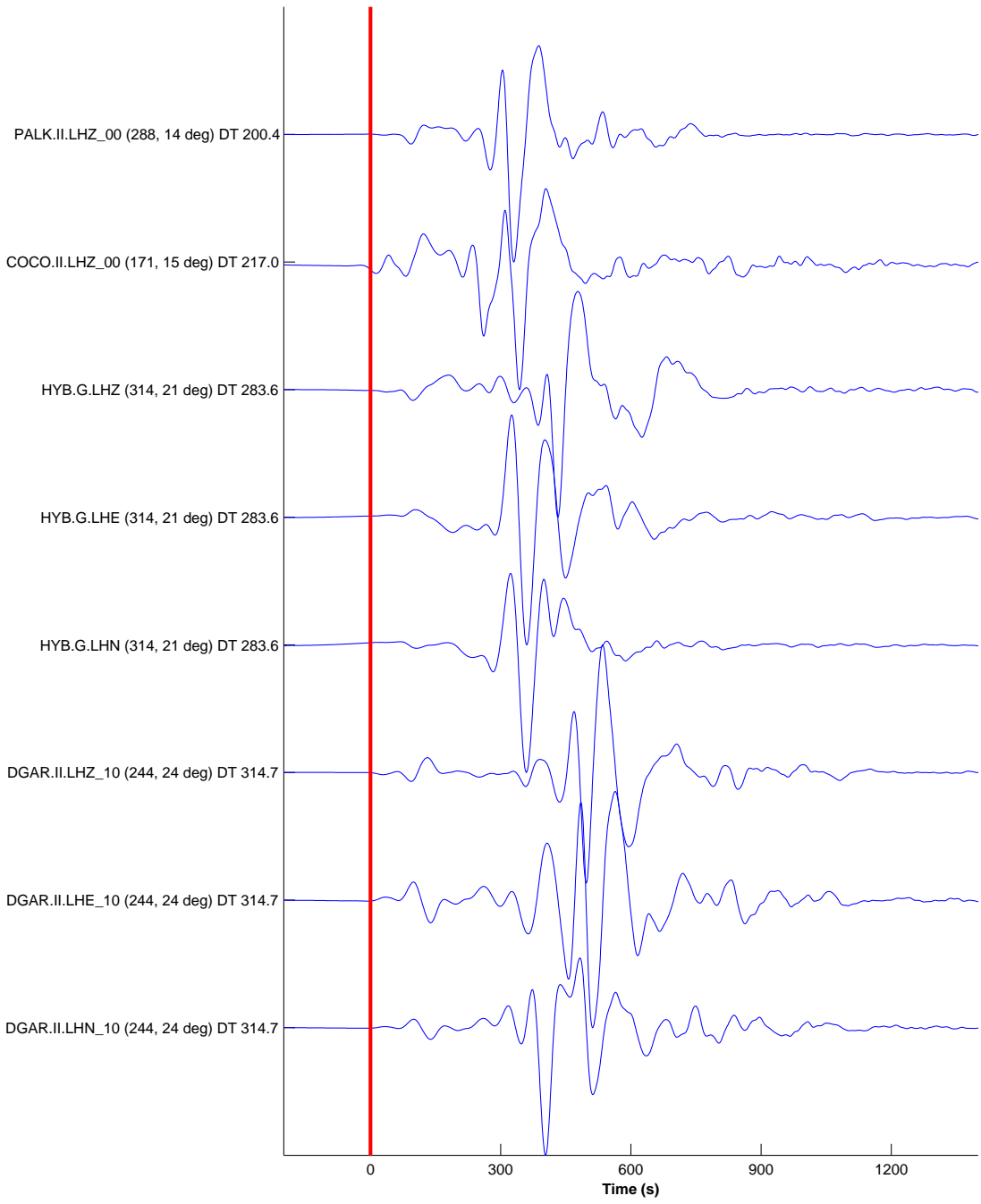


Figure S24: Displacement seismograms for near-source stations, with calibration applied only (no deconvolution), and bandpass filtered 50–500 s. Compare with Figure S25.

variable time shifts: reference time is 2004-12-26 00:58:50; PALK max -4.79e+07 nm at t = 348.5 s  
LHE LHE\_10 LHN LHN\_10 LHZ LHZ\_00 LHZ\_10 [ nm, T = 50.0–500.0 s (2.0–20.0 mHz)] event M122604A (2004-12-26, M9.0, 9° / 8 seismograms (4 stations) ordered by distance, norm --> max(abs(d\_i))

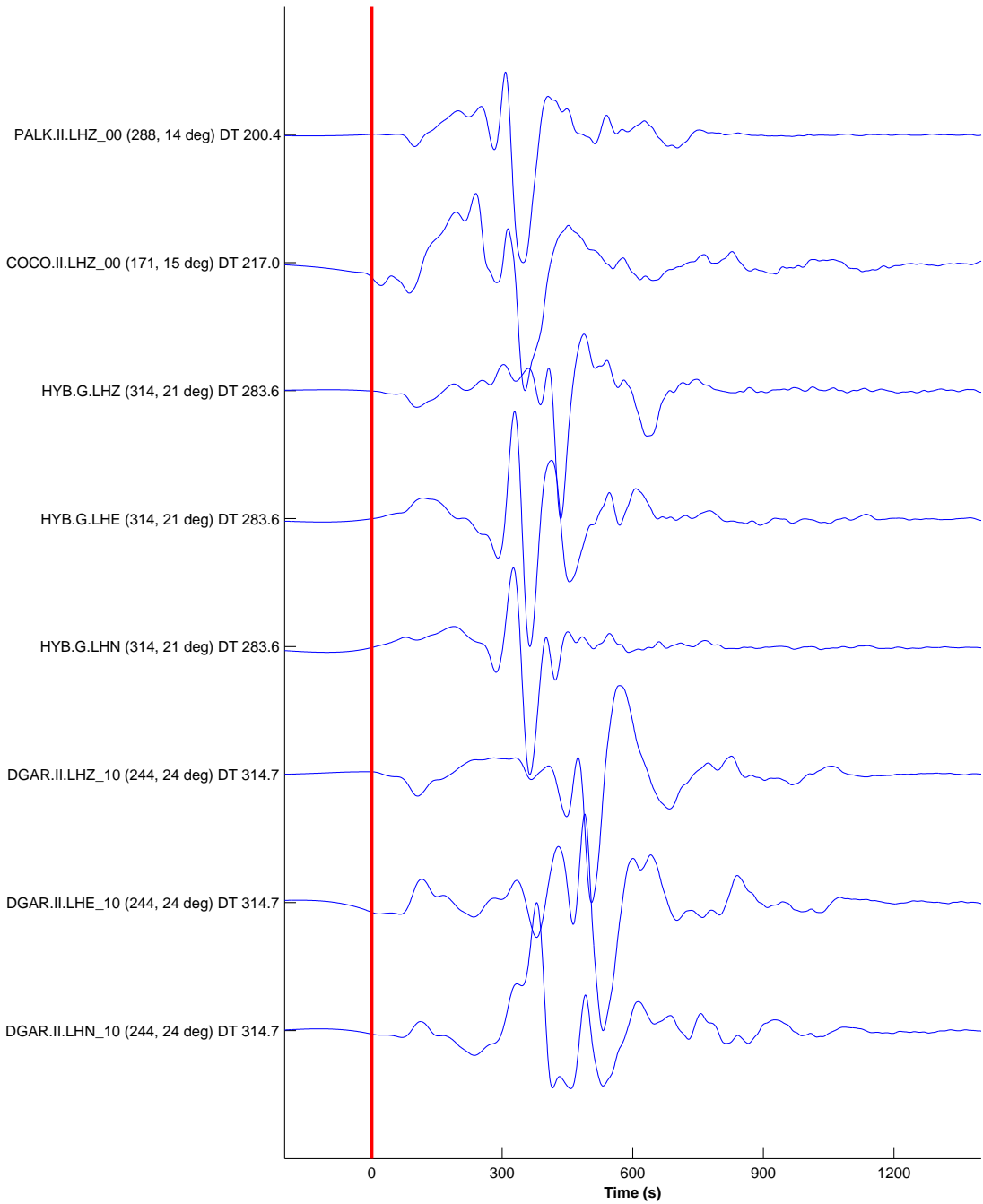


Figure S25: Displacement seismograms for near-source stations, with instrument deconvolved, and bandpass filtered 50–500 s. The waveforms are strikingly different from those in Figure S24, emphasizing the importance of deconvolution in this example. Compare with Figure S12 of *Ammon et al. (2005)*.

16 points, center at (95.78, 3.30), distance increment 30 deg

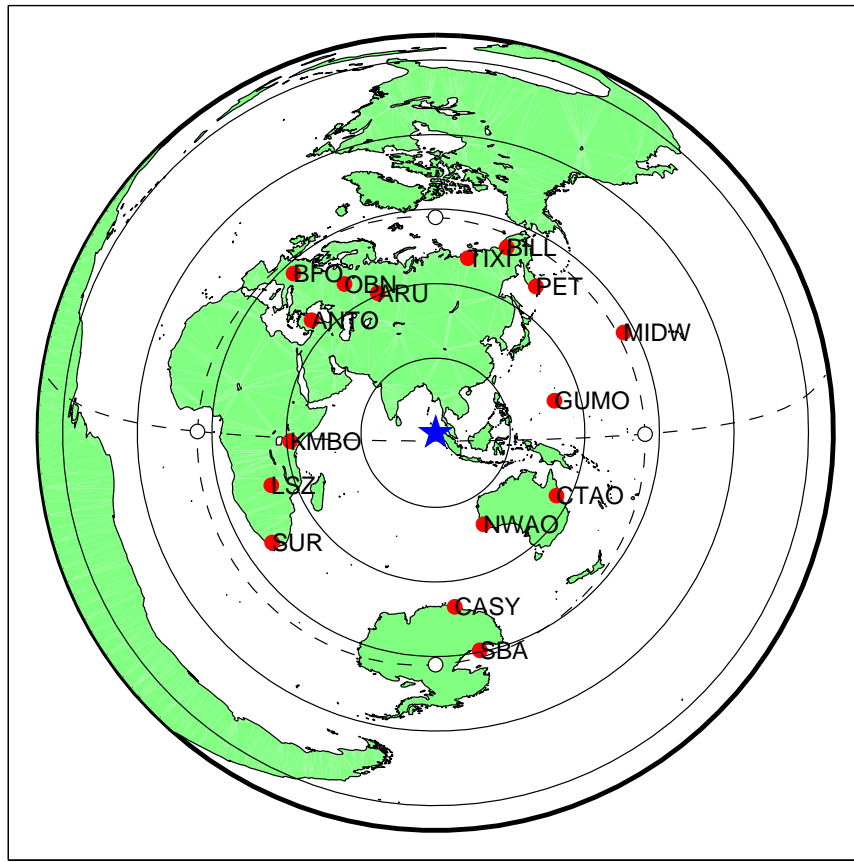


Figure S26: Stations used in Figure S27. Epicentral distances are  $35^\circ < \Delta < 90^\circ$ .

variable time shifts: reference time is 2004–12–26 00:58:50; TIXI max  $-1.96\text{e}+06$  nm at  $t = 897.0$  s  
 BHZ\_00 [ nm,  $T = 10.0\text{--}500.0$  s (2.0–100.0 mHz)] event M122604A (2004–12–26, M9.0, 95.8, 3.3,  $z = 10.0$  km)  
 16 / 16 seismograms (16 stations) ordered by azimuth, norm  $\rightarrow$  none

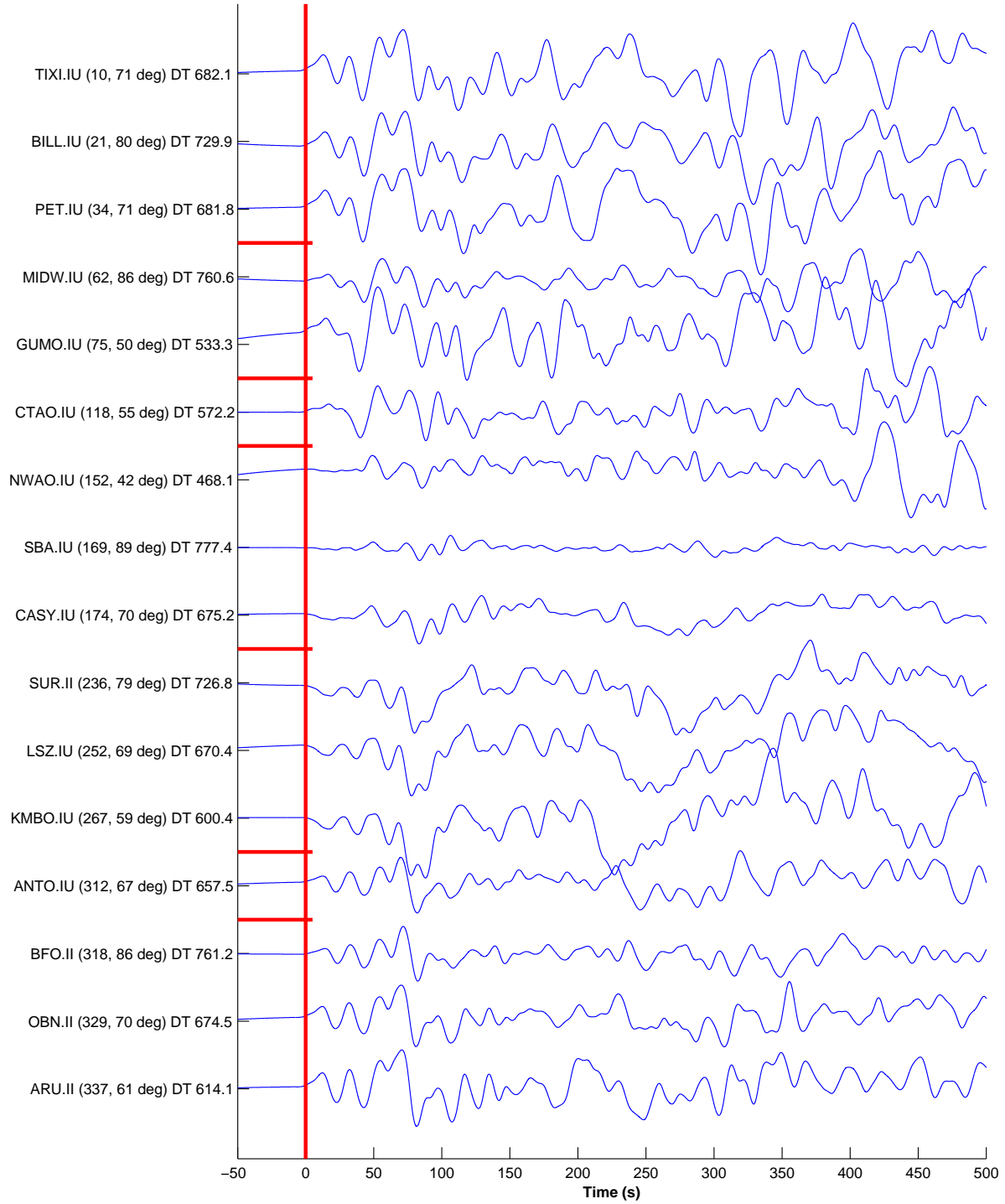


Figure S27: Reproducing Figure S11 of Ammon *et al.* (2005), showing the azimuthal variation of the P wave. Here the vertical-component displacement seismograms have been filtered between periods 10–500 s, and there is no relative scaling between seismograms.

variable time shifts: reference time is 2004–12–26 00:58:50; TIXI max  $-1.96\text{e+}06$  nm at  $t = 897.0$  s  
 BHZ\_00 [ nm,  $T = 10.0\text{--}500.0$  s (2.0–100.0 mHz) ] event M122604A (2004–12–26, M9.0, 95.8, 3.3,  $z = 10.0$  km)  
 16 / 16 seismograms (16 stations) ordered by azimuth, norm  $\rightarrow$  none

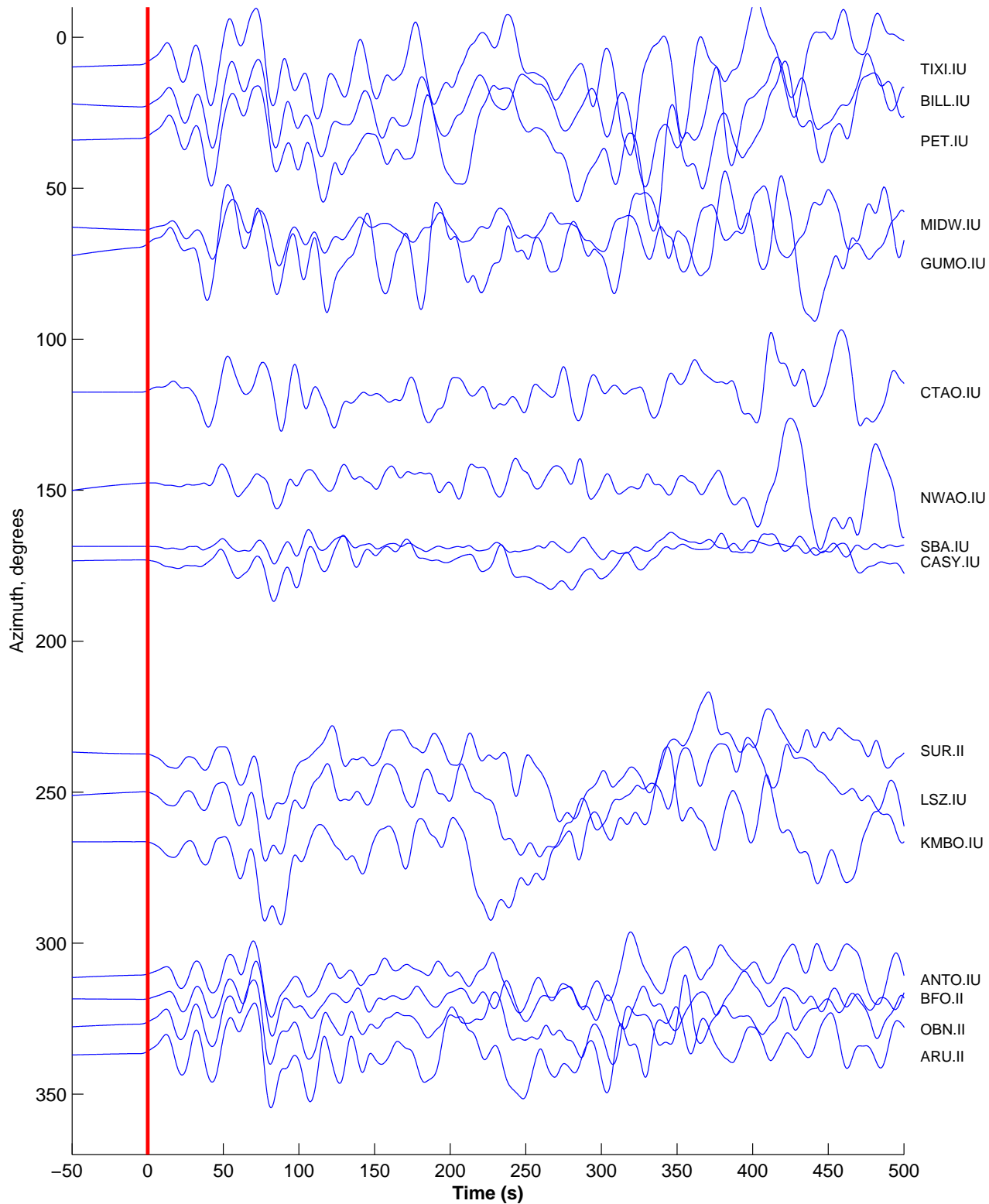


Figure S28: Same as Figure S27, but with time series plotted at their actual station azimuths.

### Questions for Problem 3-3

Modify `sumatra_hf_template.m` to filter the BHZ time series from 4–8 Hz. I suggest loading the entire data set and browsing all the stations, one seismogram at a time. Recall what we saw for CAN in the earlier homework.

1. (0.3) Show a plot and identify other stations (if any) that exhibit high-frequency, post-rupture signals that are similar to those identified at CAN.
2. (0.2) Is there anything systematic about the other stations?

Provide your interpretation of these signals.

### Solutions for Problem 3-3

1. With a global analysis, we find that CAN is not alone in exhibiting a peculiar, post-P high-frequency “bursts.” Figure S3 shows six stations that have this signal: INU.G, CAN.G, TAM.G, SCZ.G, MPG.Z, PEL.G
2. All six stations are from the Geoscope network, which points to an explanation that is unique to these six stations only. My guess was that either (1) the values of these stations were the same, and that they were somehow deforming under the dynamic strains from Sumatra; or (2) there was some error in how the data were recorded. As explained in the email below, it turned out to be a problem with the digitizers at these stations.

The interesting connection is that the signal correlates with the Sumatra surface waves, which can be seen upon comparison of Figures S3 and S4. This turned out to be a key clue in determining the source of the problem.

### Epilogue: Email to Carl from Geoscope (10/9/2012)

Our analysis in Problem 3-3 identified the peculiar high-frequency signal at six stations, all of which were in the Geoscope network. I wrote to Geoscope in October 2012, and the response from Eleanore Stutzmann is below. It turns out that the signals in Figure S3 were not signals of actual ground motion, though they are artifacts caused by large ground motions.

We never noticed the strange signal that you see. Hereafter is a possible explanation found out by the engineers in charge of the network (Nicolas Leroy and Sébastien Bonaime who were not yet working for GEOSCOPE in 2004). If anyone has other suggestion, we would be happy to know about it.

At the time of Sumatra event, the stations that you mention were equipped with a old generation digitizer ST-CCU. For this generation 16 bits was a maximum for Analog to Digital Conversion. This ST-CCU was a “false” 21 bits digitizer that built 21 samples out of 16 bits samples coming from 2 signal paths with different gains for the same signal.

A first path had a gain of 32, that allowed the noise and the small events to be sampled with a maximum resolution. The other path had a gain of 1, to allow the big events to be sampled also with a 16bit resolution.

32=2^5, 16+5=21 !

When the x32 path was saturated, the value used was only the x1 value, resulting in a different resolution (counts/V). See attached picture (Figure S5). So for any velocity value, there were only 16 useful bits but the samples were coded at the end on 21 bits. Then they were converted to Stein1 encoding and to miniseed...

We are trying to figure out what was the exact conversion procedure and if there was any post processing of the data before the conversion to Stein1. What is not clear is what piece of software decided to switch from one path to the other, or if it was just a addition of the two paths...

When you apply a 4Hz–8Hz filter, you see the quantization error that results from the resolution change. We can imagine that the quantization error is 32 times higher during the period where the signal is digitized on the second path (with gain x1).

Most of those systems have been replaced. SCZ is the last station with that kind of digitizer. At the time of Honshu event last year, only SCZ and NOUC were equipped with a ST-CCU and only these 2 stations have this strange signal.

6 points, center at (95.78, 3.30), distance increment 30 deg

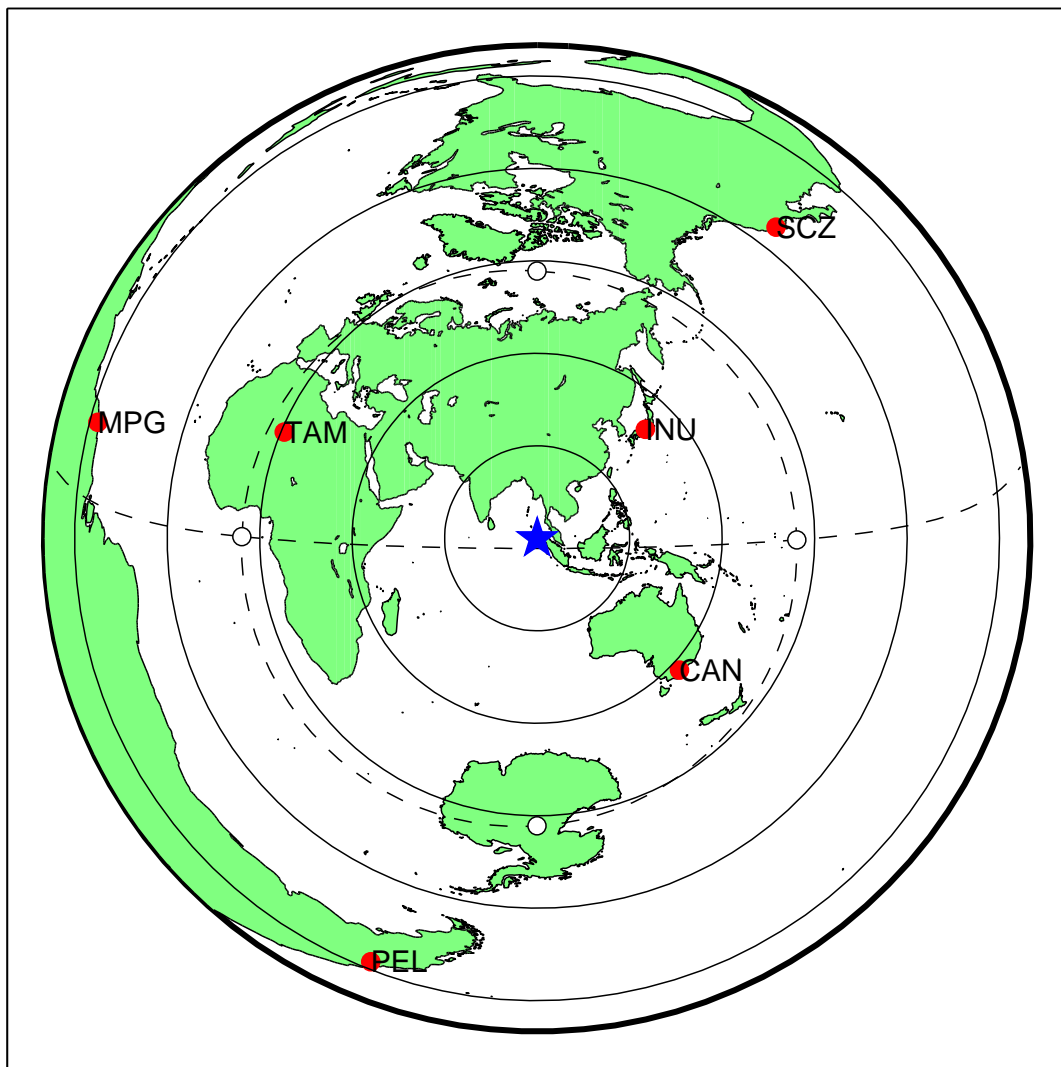


Figure S2: Map of stations in Figure S3.

2004–12–26 00:48:25 + 7687.89 s; INU max 4.21e+01 nm at t = 845.1 s  
 BHZ BHZ\_00 [ nm, T = 0.1–0.2 s (4.00–8.00 Hz)] event M122604A (2004–12–26, M9.0, 95.8, 3.3, z = 10.0 km)  
 6 / 6 seismograms (6 stations) ordered by distance, norm --> max(abs(d\_i))

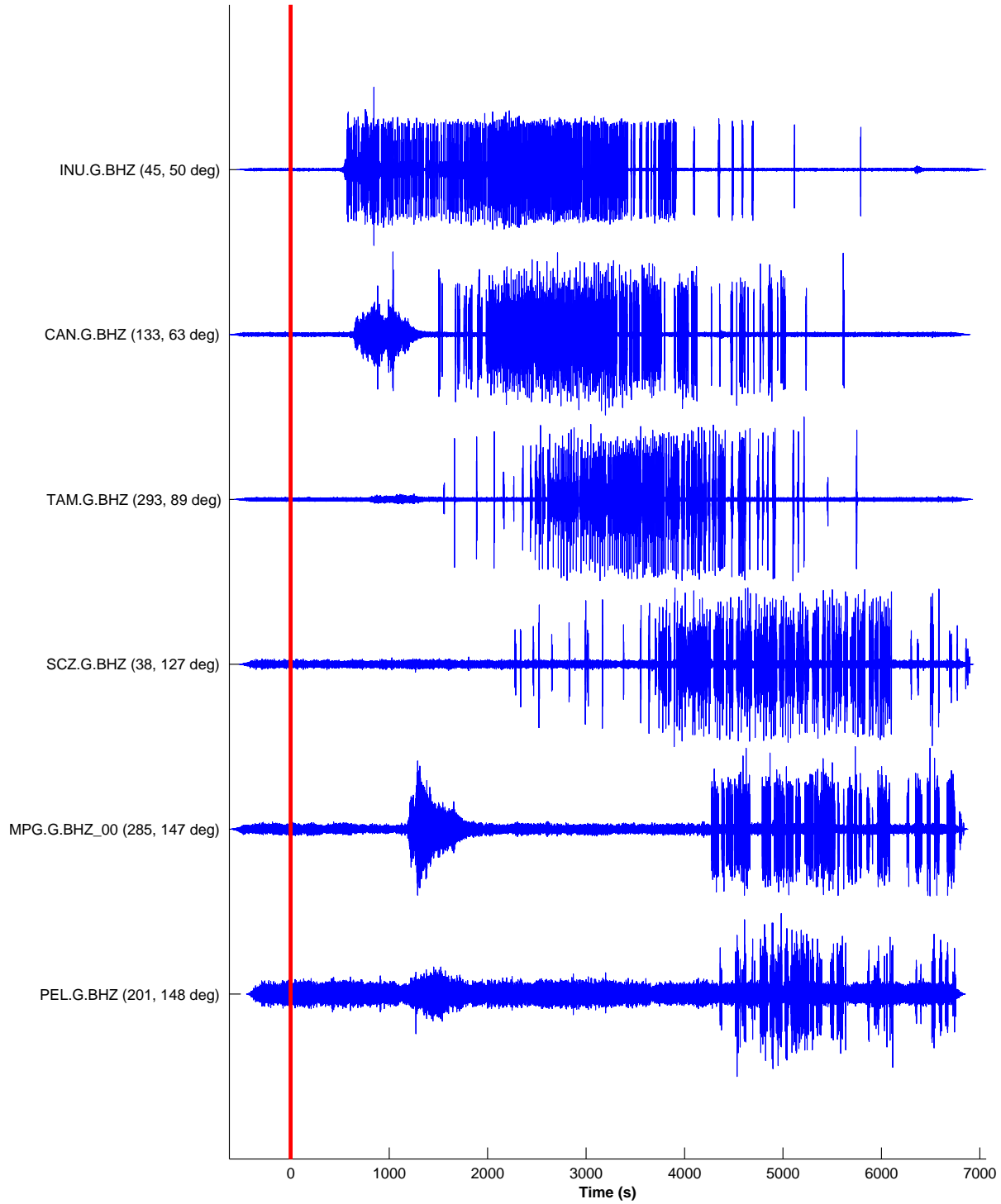


Figure S3: Peculiar post-P, high-frequency signals identified at six Geoscope stations, including CAN (Canberra). (The network code is the G in labels like CAN.G.BHZ.) Seismograms have been filtered between 4–8 Hz. Note that the “bursts” align with the passage of the dominant surface wave train (Figure S4).

2004–12–26 00:48:25 + 7687.89 s; INU max 1.01e+07 nm at t = 1959.7 s  
 BHZ BHZ\_00 [ nm, T = 10.0–30.0 s (0.03–0.10 Hz)] event M122604A (2004–12–26, M9.0, 95.8, 3.3, z = 10.0 km)  
 6 / 6 seismograms (6 stations) ordered by distance, norm --> max(abs(d\_i))

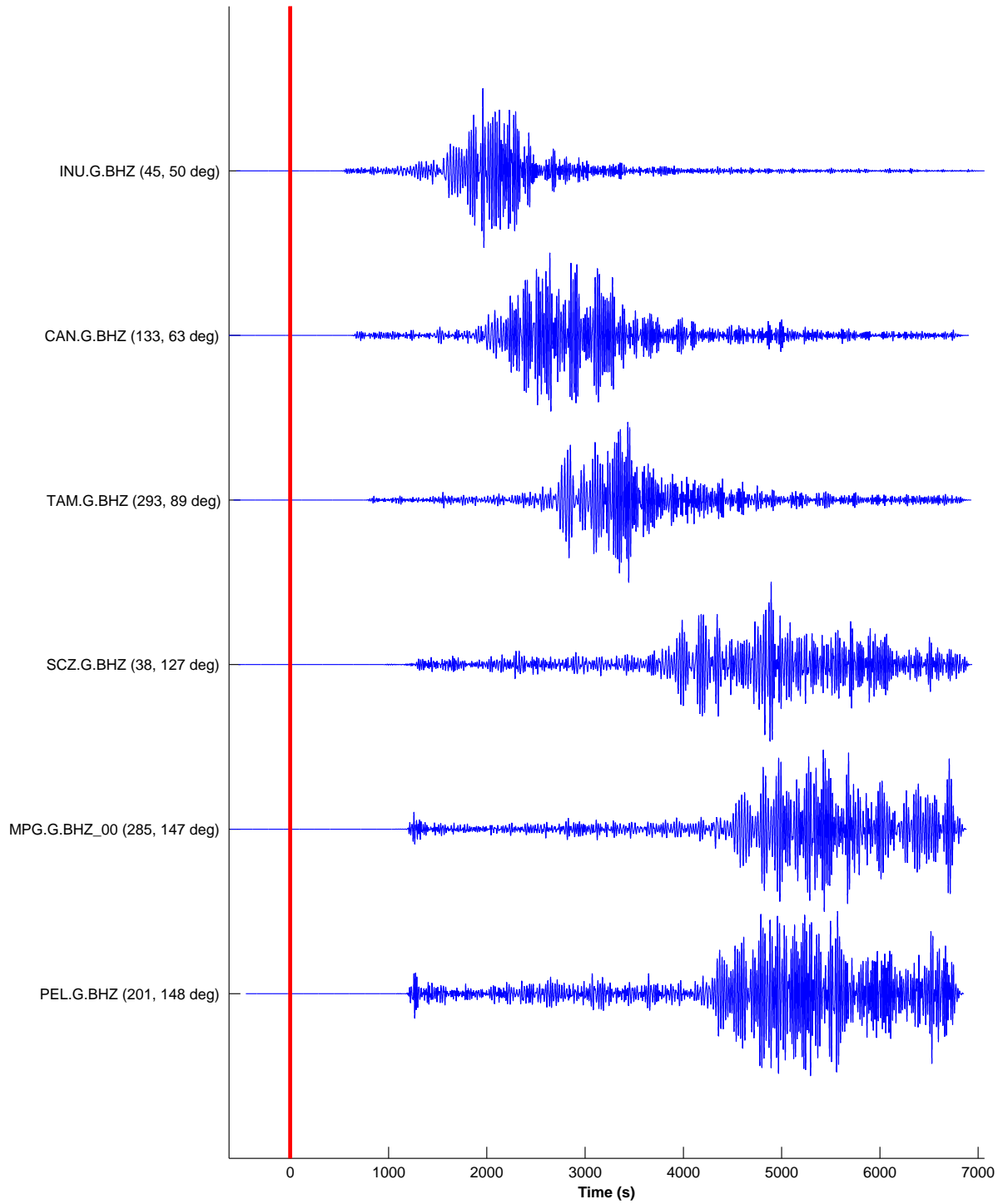


Figure S4: Same seismograms as in Figure S3, but here filtered 10–30 s to accentuate the dominant surface-wave energy in the seismograms. The surface waves are coincident in time with the high-frequency bursts in Figure S3.

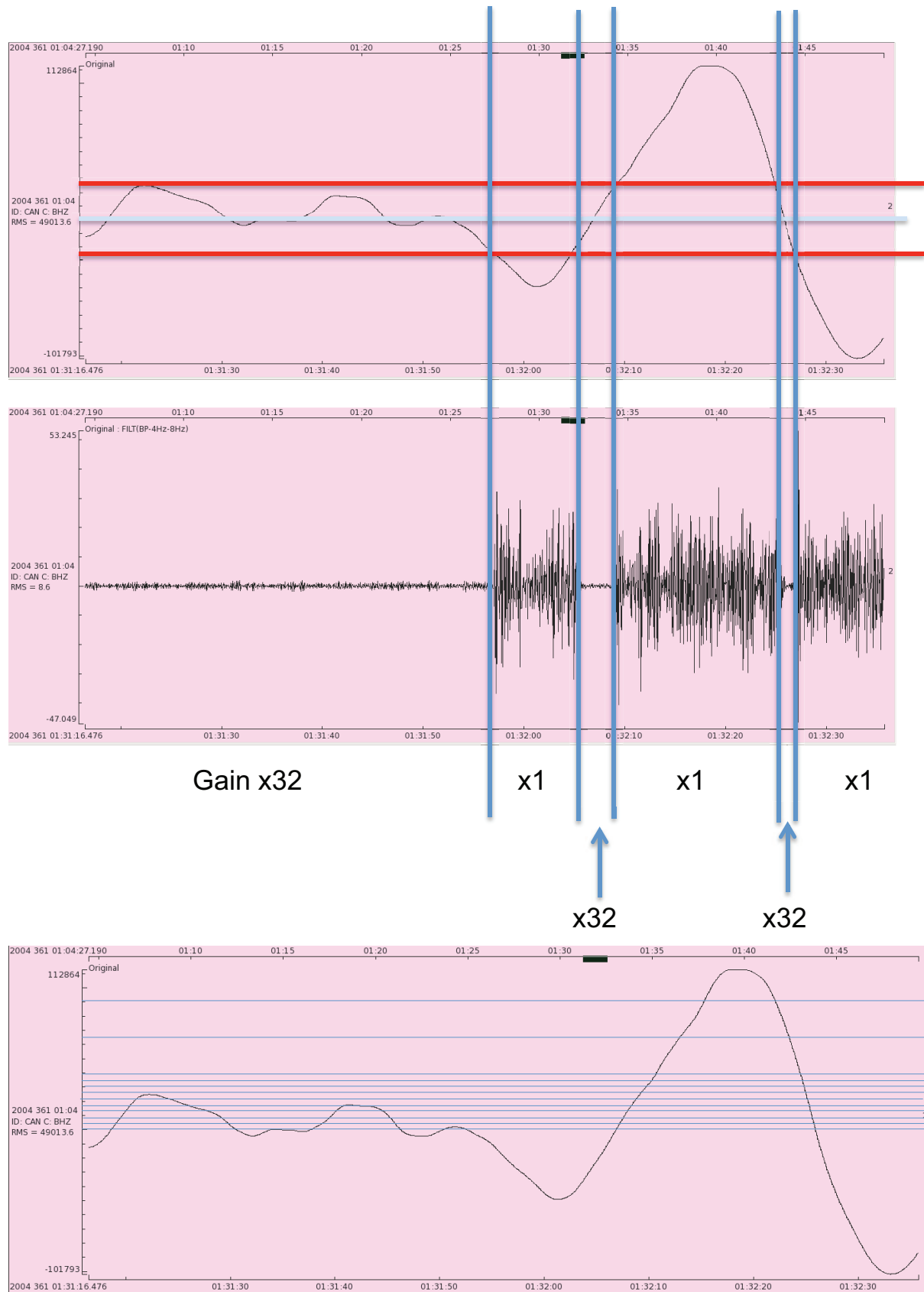


Figure S5: Figures from Eleanore Stutzmann at Geoscope.